

**CENTER OF EXCELLENCE
FOR
MATERIALS RESEARCH**

Final Progress Report

AUTHORS

**A.S. Khan, P. Centala, J.D. Humphrey,
N.T Wright, M. G. da Silva and D.J. Doss**

May 17, 1996

**U.S. Army Research Office
Grant No: DAAH04-95-2-0002**

**The University of Maryland Baltimore County
5401 Wilkens Avenue
Baltimore, MD 21228-5398**

19960910 029

**APPROVED FOR PUBLIC RELEASE; DISTRIBUTION UNLIMITED
THE VIEWS, OPINIONS, AND/OR FINDINGS CONTAINED IN THIS
REPORT ARE THOSE OF THE AUTHOR(S) AND SHOULD NOT BE
CONSTRUED AS AN OFFICIAL DEPARTMENT OF THE ARMY POSITION,
POLICY, OR DECISION, UNLESS SO DESIGNATED BY OTHER
DOCUMENTATION**

DTIC QUALITY INSPECTED 8

REPORT DOCUMENTATION PAGE

Form Approved
OMB NO. 0704-0188

Public reporting burden for this collection of information is estimated to average 1 hour per response, including the time for reviewing instructions, searching existing data sources, gathering and maintaining the data needed, and completing and reviewing the collection of information. Send comment regarding this burden estimate or any other aspect of this collection of information, including suggestions for reducing this burden, to Washington Headquarters Services, Directorate for Information Operations and Reports, 1215 Jefferson Davis Highway, Suite 1204, Arlington, VA 22202-4302, and to the Office of Management and Budget, Paperwork Reduction Project (0704-0188), Washington, DC 20503.

1. AGENCY USE ONLY (Leave blank)		2. REPORT DATE May 17, 1996		3. REPORT TYPE AND DATES COVERED Final Progress Report	
4. TITLE AND SUBTITLE Center of Excellence for Materials Research				5. FUNDING NUMBERS DAAH04-95-2-0002	
6. AUTHOR(S) A.S. Khan, P. Centala, J.D. Humphrey, N.T. Wright, M. G. da Silva and D.J. Doss					
7. PERFORMING ORGANIZATION NAMES(S) AND ADDRESS(ES) The University of Maryland Baltimore County Department of Mechanical Engineering Baltimore, MD 21228-5398				8. PERFORMING ORGANIZATION REPORT NUMBER	
9. SPONSORING / MONITORING AGENCY NAME(S) AND ADDRESS(ES) U.S. Army Research Office P.O. Box 12211 Research Triangle Park, NC 27709-2211				10. SPONSORING / MONITORING AGENCY REPORT NUMBER ARO 32609.1-M5	
11. SUPPLEMENTARY NOTES The views, opinions and/or findings contained in this report are those of the author(s) and should not be construed as an official Department of the Army position, policy or decision, unless so designated by other documentation.					
12a. DISTRIBUTION / AVAILABILITY STATEMENT Approved for public release; distribution unlimited.				12 b. DISTRIBUTION CODE	
13. ABSTRACT (Maximum 200 words) This report includes two projects that were funded under Center of Excellence for Materials Research. In case of Thermomechanics of Fiber-Reinforced Composites, a new apparatus to perform multiaxial thermomechanical tests on small samples has been developed. This report includes our design process, that is, the theoretical ideas and developments that motivated the overall design, the preliminary tests that verified some early hypotheses, the various design alternatives that were considered, and details on the final system that was assembled. In the second project entitled "High Strain-Rate Behavior and Damage Measurements in Glass-Reinforced Plastics", experimental results are reported over a wide range of strain-rate and in test samples of three orientations. Elastic constants and strengths in two orientations in direction of woven fibers and one perpendicular direction, are reported along with failure mechanisms during quasi-static and impact loading of this material.					
14. SUBJECT TERMS Thermomechanics, composites, elastomers, Glass reinforced-plastic visco-elastic behavior, strain-rate dependence.				15. NUMBER OF PAGES 55	
				16. PRICE CODE	
17. SECURITY CLASSIFICATION OR REPORT UNCLASSIFIED	18. SECURITY CLASSIFICATION OF THIS PAGE UNCLASSIFIED	19. SECURITY CLASSIFICATION OF ABSTRACT UNCLASSIFIED	20. LIMITATION OF ABSTRACT UL		

TABLE OF CONTENTS

I. THERMOMECHANICS OF FIBER-REINFORCED COMPOSITES

a.	Preface	1
b.	Introduction	1
c.	Theoretical Framework	2
d.	A Feasibility Experiment	9
e.	Numerical Simulations	10
f.	Experimental System	14
g.	Conclusions	22
h.	References	22

II. HIGH STRAIN-RATE BEHAVIOR AND DAMAGE MEASUREMENTS IN GLASS REINFORCED PLASTICS

a.	Abstract	37
b.	Introduction	38
c.	Experimental Procedures	40
	(i) Material	40
	(ii) Quasi-static Compression Tests	41
	(iii) Dynamic Response Experiments	43
d.	Results & Discussion	43
	(i) Quasi-Static Response	43
	(ii) Dynamic Response	51
e.	Conclusions	53
f.	References	54

THERMOMECHANICS OF FIBER-REINFORCED COMPOSITES

J.D. Humphrey, N.T. Wright, M.G. da Silva and D.J. Doss

Department of Mechanical Engineering
The University of Maryland
Baltimore MD 21228-5398

PREFACE

Our long term goal is to identify multiaxial phenomenological constitutive relations for the finite strain, thermomechanical behavior of unswollen and swollen fiber-reinforced elastomers. Toward this end, we originally proposed to perform combined finite extension and torsion tests on fairly large elastomeric specimens (15 cm long x 5 cm diameter) using our existing MTS BIONIX® load frame; thermal properties were also to be measured using standard techniques so as to facilitate quantification of the thermal histories during thermoelastic testing. Based on discussions with ARL personnel (soon after notification of funding), however, it became apparent that it was preferred that we develop a capability to perform multiaxial thermomechanical tests on small samples in order to evaluate new candidate elastomers as they are developed. Hence, the scope of the work was so modified. Because our final design and subsequent results will be reported in refereed publications, the primary purpose of this report is to document our design process, that is, the theoretical ideas and developments that motivated the overall design, the preliminary tests that verified some early hypotheses, the various design alternatives that were considered, and details on the final system that was assembled. In this way, this final report will complement subsequent journal articles; together, they will provide complete documentation of this project.

INTRODUCTION

It is well known that the properties of elastomers are highly dependent on temperature level, ranging from below the glass transition temperature T_g to above the melting temperature T_m . In this research, we focus on the behavior between T_g and T_m , that is in the rubbery range. A distinguishing feature of elastomers within $T \in (T_g, T_m)$ is their "high elasticity", that is their ability to

undergo large elastic deformations. Not surprisingly, there is a huge literature on the finite strain thermoelastic behavior of "rubber-like" materials. The earliest such paper is that of Gough (1805), results of which were latter confirmed and extended by Joule (1859). In particular, Gough and Joule showed that elastomers exhibit "peculiar" (i.e., in comparison to traditional engineering materials such as metals) behaviors: for example, rubber warms when stretched adiabatically, and it shrinks when heated. Although a thermoelastic theory was proposed by Kelvin (1857) for elastomers, suitable theoretical work had to await a more fundamental understanding of the long-chain polymeric structure of elastomers (which developed significantly from 1926 through 1943 due to work by Ostwald, Mark, Meyer, Guth, Flory, Treloar, and others) and advances in modern continuum mechanics (which developed largely in the 1950s and 1960s due to work by Rivlin, Noll, Coleman, Green, Ericksen, Truesdell, and others). See Treloar (1975) and Truesdell and Noll (1965), respectively, for a complete discussion of these developments. More recently, phenomenological finite strain thermoelastic theories were advanced by Chadwick (1974), Chadwick and Creasy (1984), Ogden (1992) and others. These will be discussed below. It should be noted, however, that the latter authors point out that the primary reason that well accepted descriptors of the finite strain thermoelastic behavior of elastomers remain elusive is the lack of complete multiaxial experimental data.

It is similarly well known that elastomers are moderate thermal conductors, that is, reported values of the thermal conductivity are three or more orders of magnitude smaller than those for metals. As with most materials, however, the thermal conductivity of elastomers varies with the temperature level (e.g., Dashora, 1994). Schapery and Martin (1974) and Burland et al. (1989) also report some findings on the thermophysical properties (e.g., thermal diffusivity) of particulate filled elastomers. Nonetheless, there is relatively little data on the thermophysical properties of elastomers as a function of multiaxial finite strain, swelling, reinforcement by polymeric fibers, etc.

The goal of this work was to develop a theoretically-motivated test system capable of providing much needed multiaxial thermoelastic and thermophysical data on elastomers subject to a broad range of finite strains, temperature levels, and environmental conditions. This technical report begins with a review of the theoretical motivation, and then documents the experimental design.

THEORETICAL FRAMEWORK

General Concepts

Coleman and Gurtin (1967) proposed a theoretical construct for identifying general constitutive functions that can be used to quantify the behavior of a nonlinearly elastic, heat conducting material. Their theory is briefly reviewed here, albeit with some modifications and notational changes. They suggested that a general thermodynamic process can be described by the following fields: the current mass density ρ , body force b , internal heat generation g , Helmholtz free energy ψ , entropy η , first Piola-Kirchhoff stress P , referential heat flux q_0 , motion x of material particles within the

body, and temperature T , all of which can vary, in general, as a function of the initial position X within the body and time t (note that b , ψ , g are defined per unit mass). Coleman and Gurtin suggested that ρ , b , and g can be found by solving the balance equations for mass, linear momentum, and energy, which in referential form are,

$$\det F = \frac{\rho_0}{\rho}, \quad F = \frac{\partial x}{\partial X} \quad (1)$$

and $J = \det F$, F is the deformation gradient tensor, and ρ_0 the mass density in the reference configuration,

$$\nabla_0 \cdot P + \rho_0 b = \rho_0 \ddot{x}, \quad \text{where } P = J F^{-1} \cdot t \quad (2)$$

and $\nabla_0 = \partial(\)/\partial X$, $(\ddot{\ }) = d^2(\)/dt^2$, $(\)^{-1}$ denotes inverse of the tensor, t is the Cauchy (or true) stress, and

$$\rho_0 \dot{\epsilon} = P^T : \dot{F} - \nabla_0 \cdot q_0 + \rho_0 g, \quad \text{where } q_0 = J F^{-1} \cdot q \quad (3)$$

ϵ is the internal energy, q is the spatial heat flux vector, and $(\)^T$ denotes transpose of the tensor. Coleman and Gurtin further noted that the free energy, entropy, stress and heat flux must be determined from the state variables (x and T , and derivatives thereof) via constitutive relations. For a local elastic theory (e.g., rate independent), appropriate state variables for a homogeneous material are F , T and $\nabla_0 T$. Hence by the principle of equipresence, general (referential) constitutive relations are

$$\psi = \hat{\psi}(F, T, \nabla_0 T), \quad \eta = \hat{\eta}(F, T, \nabla_0 T), \quad (4)_1$$

$$P = \hat{P}(F, T, \nabla_0 T), \quad q_0 = \hat{q}_0(F, T, \nabla_0 T) \quad (4)_2$$

where the $(\hat{\ })$ delineates between the function and the value of the function (left hand sides). This understood, the "hat" notation is dropped hereafter. The balance of angular momentum and the second law of thermodynamics (e.g., Clausius-Duhem inequality) provide restrictions on these constitutive functions. In referential form, these laws are

$$F \cdot P = P^T \cdot F^T \quad (5)$$

and,

$$-\rho_0 (\dot{\psi} + \eta \dot{T}) + P^T : \dot{F} - \frac{1}{T} q_0 \cdot \nabla_0 T \geq 0. \quad (6)$$

Equation 6 reveals that ψ cannot depend on $\nabla_0 T$, and that the four constitutive functions are not all independent. Rather,

$$P = \rho_0 \frac{\partial \psi}{\partial F^T}, \quad \eta = - \frac{\partial \psi}{\partial T}. \quad (7)$$

Hence, the stress and entropy must also be independent of the temperature gradient, and we only need to identify specific forms of the free energy and the heat flux in order to have a complete constitutive formulation. Finally, the principle of material frame indifference requires that ψ and q_0 depend on F only through U , a pure deformation, which renders the constitutive relations invariant to rigid body motion (recall the polar decomposition theorem, $F = R \cdot U$, where the orthogonal tensor R represents rigid body motion). Because the right Cauchy-Green deformation tensor C equals

U^2 , however, ψ and q_o can be equivalently written in terms of C ($=F^T \cdot F$). Hence we need only identify specific functional forms of

$$\psi = \psi(C, T), \quad q_o = q_o(C, T, \nabla_o T), \quad (8)$$

and the associated values of the material parameters. It is useful, therefore, to note that

$$P = 2\rho_o \frac{\partial \psi}{\partial C} \cdot F^T \quad (9)$$

is easier to employ than equation 7₁. Moreover, if the material is initially isotropic with respect to the reference configuration, equation 8 reduces to

$$\psi = \psi(I_C, II_C, III_C, T), \quad q_o = q_o(I_C, II_C, III_C, T, \nabla_o T), \quad (10)$$

where the principal invariants of C are given by

$$I_C = \text{tr} C, \quad 2II_C = (\text{tr} C)^2 - \text{tr} C^2, \quad III_C = \det C. \quad (11)$$

Similar relations exist for transversely-isotropic and orthotropic symmetries (Spencer, 1984), which may result from embedding fibers in a homogeneous elastomeric matrix. Nonetheless, the goal of this project was to design and construct an experimental system for identifying forms of the free energy and heat flux consistent with equation 8 via tests on small samples.

In experimental mechanics, one always seeks a boundary value problem that yields the most easily and reliably interpreted data. For finite strains, experimental configurations of choice include the in-plane biaxial extension of thin sheets of material, combined extension and torsion of solid cylinders, inflation of membranes, and combined extension, inflation and torsion of thick-walled hollow tubes (we have experience with each of these configurations, as applied to testing biological tissues). Of these experiments, however, the simplest to interpret is the in-plane biaxial test, which is the focus herein.

Form of the free energy

Ogden (1992) presented an approach for inferring the form of ψ from biaxial tests, but have we developed an alternate approach which exploits the near incompressibility of elastomers under isothermal conditions. Note, therefore, that isothermal deformation induced volume changes in elastomers are typically $O(10^{-4})$, whereas temperature-induced volume changes are of $O(10^{-4})$ per $^{\circ}\text{C}$ (see Wood and Martin, 1962). Hence, the latter will be two orders of magnitude greater for a 100°C change. To exploit this, consider the case of an initially isotropic thermoelastic elastomer that is first uniformly heated from a reference temperature T_o to a $T > T_o$, and then stretched biaxially (see Humphrey, 1996 for details of this case as well as the case of stretch followed by heating). Moreover, let the homogeneous temperature-induced and load-induced deformations (Figure 1) be given by $F_1 = \Lambda I$ and $F_2 = \text{diag}[\lambda_1, \lambda_2, \lambda_3]$, respectively, where Λ and λ_i are stretch ratios, $\det F_1 \neq 1$, but $\det F_2 = 1$. Hence, one only needs to measure Λ , due to changes in temperature, and λ_1 and λ_2 , due to in-plane loads (with $\lambda_3 = 1/(\lambda_1 \lambda_2)$). Of course, the total deformation is given by $F = F_2 \cdot F_1$ and thus $C = F_1^T \cdot C_2 \cdot F_1$, with $C_2 = F_2^T \cdot F_2$. Now, since $\det C = \det C_1 \det C_2 =$

$\det C_1$, equations 2₂, 9, and 10₁ yield (using the chain rule)

$$t = 2\rho (III_{C_1} \frac{\partial \Psi}{\partial III_{C_1}} I + (\frac{\partial \Psi}{\partial I_C} + I_C \frac{\partial \Psi}{\partial II_C}) B - \frac{\partial \Psi}{\partial II_C} B^2) - pI \quad (12)$$

where p is a Lagrange multiplier that enforces the constraint $\det C_2 = 1$, and $B = F \cdot F^T$. Equation 12 is the stress-stretch-temperature relation. In-plane, quasi-static, biaxial stretching in the absence of body forces results in a homogeneous plane stress field ($t_{i3} = 0$, $i=1,2,3$) in the central region of the specimen, thus equilibrium (equation 2₁) simply requires that p is a constant at each F_2 . The non-zero components of the Cauchy stress are, therefore,

$$t_{11} = 2\rho \Lambda^2 (\lambda_1^2 - \lambda_3^2) (\frac{\partial \Psi}{\partial I_C} + \Lambda^2 \lambda_2^2 \frac{\partial \Psi}{\partial II_C}), \quad (13)_1$$

$$t_{22} = 2\rho \Lambda^2 (\lambda_2^2 - \lambda_3^2) (\frac{\partial \Psi}{\partial I_C} + \Lambda^2 \lambda_1^2 \frac{\partial \Psi}{\partial II_C}). \quad (13)_2$$

These results represent 2 equations in terms of 2 yet unknown response functions (i.e., derivatives of Ψ), and can be solved in terms of experimentally "measurable" quantities ($\Lambda, \lambda_i, t_{ij}$), namely

$$\rho \frac{\partial \Psi}{\partial I_C} (I_C, II_C, III_{C_1}, T) = \frac{1}{2\Lambda^2 (\lambda_1^2 - \lambda_2^2)} (\frac{\lambda_1^2 t_{11}}{(\lambda_1^2 - \lambda_3^2)} - \frac{\lambda_2^2 t_{22}}{(\lambda_2^2 - \lambda_3^2)}) \quad (14)_1$$

$$\rho \frac{\partial \Psi}{\partial II_C} (I_C, II_C, III_{C_1}, T) = \frac{1}{2\Lambda^4 (\lambda_2^2 - \lambda_1^2)} (\frac{t_{11}}{(\lambda_1^2 - \lambda_3^2)} - \frac{t_{22}}{(\lambda_2^2 - \lambda_3^2)}). \quad (14)_2$$

Although these response functions depend on four state variables, only two of these (I_C and II_C) change with F_2 , and thus one can vary these independently (at each T) via traditional "constant invariant tests" (Humphrey et al., 1990; Rivlin and Saunders, 1951), that is, I_C can be maintained constant at multiple prescribed values while II_C is varied, and vice versa. When there is no initial heating from T_0 (i.e., $F_1 \equiv I$), this protocol reduces to the now classical case derived by Rivlin and Saunders. Hence, aside from the same caveats that exist in isothermal protocols (e.g., sensitivity of results to experimental errors at low strain, where I_C and II_C are nearly equal), equations 14_{1,2} allow one to determine the form of the response functions at multiple temperatures directly from data. Note that $\partial \Psi / \partial III_{C_1}$ can be found from $\text{tr} t = 0$, for $F = F_1$. That is,

$$\frac{\partial \Psi}{\partial I_{C_1}} + 2\Lambda^2 \frac{\partial \Psi}{\partial II_{C_1}} + \Lambda^4 \frac{\partial \Psi}{\partial III_{C_1}} = 0. \quad (15)$$

It appears we are the first to exploit this decomposition of F , and thus the mechanical incompressibility constraint.

One final observation with regard to finding the temperature dependence of Ψ . Chadwick (1974), and later Ogden (1992), showed that (by twice integrating the specific heat $c_F = -T \partial^2 \Psi / \partial T^2$ with respect to T , at a constant F) equation 8₁ can be written as,

$$\Psi = \Psi(C, T_0) \frac{T}{T_0} + \epsilon(C, T_0) (1 - \frac{T}{T_0}) + \int_{T_0}^T c_F(C, \zeta) (1 - \frac{T}{\zeta}) d\zeta \quad (16)$$

where $\Psi = \epsilon - \eta T$ and ζ is a dummy variable. That is, a form of $\Psi(C, T)$ can be determined by knowing Ψ and ϵ from isothermal

mechanical tests at T_0 as well as $c_F(C, T)$. Equation 16 was motivated by the desire to delineate between entropic and energetic contributions to rubber-elasticity, which is essential in the formulation of structurally based constitutive relations (i.e., via statistical mechanics, see Treloar, 1975). We submit, however, that although statistical models are useful in principle, the many simplifying assumptions currently required to formulate such relations severely compromise their interpretive value. Hence, our focus is on phenomenological (ie, continuum) relations that are useful for engineering design and analysis (e.g., finite element analyses). For this reason, observe that equation 16 can be re-written as

$$\psi = \delta_1(C, T_0) + \delta_2(C, T_0) T + \delta_3(C, T_0, T) \quad (17)$$

where δ_i are scalar-valued functions that can be determined phenomenologically: δ_1 and δ_2 can be found from isothermal mechanical tests at T_0 , and δ_3 can be determined from measurements of c_F at multiple F and T . δ_3 will depend primarily on T , indeed it provides the only nonlinear temperature dependence to the free energy. Equation 17 is consistent with all current thermoelastic data (almost all of which are uniaxial), which reveal that elastomers exhibit predominantly linear stress-temperature responses at constant strains (e.g., Anthony et al, 1942). We submit that equation 17 will facilitate the quantification and evaluation of stress-strain-temperature relations and expressions for the entropy. In particular, we will now be able to compare results from isothermal tests at multiple temperatures (equations 14, 15) with combined results from isothermal tests at T_0 and measurements of $c_F(C, T)$.

Form for the heat flux

Fourier's model for heat conduction is a good descriptor for most homogeneous materials (despite a theoretically unappealing infinite speed of heat diffusion). The common form of this model is $q = -k(T) \nabla T$, where k is an isotropic scalar thermal conductivity and $\nabla T = \nabla_0 T \cdot F^{-1}$; this (spatial) equation assumes that k is independent of strain, which is not true in general. Hence, we consider a generalized Fourier's relation,

$$q_0 = -K(C, T) \cdot \nabla_0 T, \quad K(C, T) = \delta_4(C, T) I + \delta_5(C, T) C + \delta_6(C, T) C^2 \quad (18)$$

where the form¹ for the referential conductivity tensor K follows Mueller (1985), and the general dependence on C can be replaced with the appropriate invariants (see equation 10₂). The importance of this approach (which has not been exploited experimentally) is that one reduces the search for a tensor-valued function $K(C, T)$ to a search for three scalar-valued functions δ_i , which is much simpler. Note, that K cannot be measured directly via transient

¹ The Cayley-Hamilton theorem for second order tensors reveals that this form is a complete polynomial expression.

experiments, rather in such tests it must be inferred from the thermal diffusivity $\alpha_o (=K/\rho_o c_F)$.

Measurement of thermal diffusivity

The (referential) thermal diffusivity α_o can be "measured" by solving the energy equation (equation 3₁) for a tractable experimental configuration. Clearly, the energy equation is easier to solve for the case of zero stress-power (which can be achieved by maintaining the in-plane stretches constant in a plane stress configuration) and zero internal heat generation. In this case, Dillon (1962) showed that equation 3₁ becomes,

$$\rho_o c_F \dot{T} = -\nabla_o \cdot \mathbf{q}_o, \text{ where } c_F = -T \frac{\partial^2 \Psi}{\partial T^2} \quad (19)$$

and thus equations 18 and 19 yield a general governing differential equation from which the thermal diffusivity can be found. That is, $\partial T / \partial t = \alpha_o : \nabla_o (\nabla_o T)$. Except for the simplest experiments (e.g., 1-D heat conduction), however, this equation is most easily solved numerically (unlike the thermoelastic equilibrium equation which was solved trivially for the biaxial stretching configuration).

Although there are several experimental approaches for finding α_o , it appears that the *flash method* is preferred for materials of moderate conductivity that may experience thermal damage if maintained at supra-normal temperatures for long times. That is, the short-lived, small temperature rise required for the flash method is less likely to induce thermal degradation of the material; moreover, the flash method is much better suited for combination with testing at multiple finite biaxial strains because it is a non-contact method. Briefly, then, note that in the flash method one subjects a thin specimen to a short burst of radiant energy on one face and then measures the associated temperature history on the opposite, non-illuminated face. Introduced by Parker et al. (1961), the flash method was originally used to measure the out-of-plane thermal diffusivity by subjecting the specimen to an uniform illumination (Figure 2a). Later, however, Maillet et al. (1990) and Lachi and Degiovanni (1991) showed that the out-of-plane and one in-plane component can be measured simultaneously if the specimen is illuminated through a circular aperture (Figure 2b).

In the case of uniform illumination (i.e., Parker's original method), one can obtain an analytic expression for the out-of-plane component of the diffusivity in terms of experimentally measurable quantities. Briefly, the 1-D energy equation for heat flow in the out-of-plane (i.e., 3) direction is (from equation 19)

$$\frac{\partial T}{\partial t} = (\alpha_o)_{33} \frac{\partial^2 T}{\partial X_3^2}, \quad (20)$$

where $X_3 \in [0, H]$, and H is the undeformed thickness. An analytic expression for the rise in the rear surface temperature $T(H, t)$ is (Carslaw and Jaeger, 1959)

$$T(H, t) = \frac{Q}{\rho_o c_F H} \left[1 + 2 \sum_{n=1}^{\infty} (-1)^n \exp \left(\frac{-n^2 \pi^2}{H^2} (\alpha_o)_{33} t \right) \right] \quad (21)$$

where Q denotes the pulse of radiant energy. Two dimensionless parameters, ϕ and ω of use are

$$\phi(H, t) = \frac{T(H, t)}{T_M}, \quad \omega = \frac{\pi^2 (\alpha_o)_{33} t}{H^2}, \quad (22)$$

where T_M is the maximum temperature seen on the non-illuminated face. Equation 21 can thus be re-written as,

$$\phi = 1 + 2 \sum_{n=1}^{\infty} (-1)^n \exp(-n^2 \omega), \quad (23)$$

which is a convergent series. Parker et al. suggested that this equation be solved for $\phi=0.5$, which yields $\omega=1.38$. Hence, the out-of-plane thermal diffusivity can be measured (at multiple strains and ambient temperatures) via²,

$$(\alpha_o)_{33} = \frac{1.38 H^2}{\pi^2 t_{1/2}}, \quad (24)$$

where $t_{1/2}$ is the time required for the non-illuminated surface to reach half of its maximum temperature (Figure 3). Although this 1-D analysis assumes insulated edges, and that the thermal diffusivity is independent of temperature, these are not severe restrictions. For example, the temperature rise is typically small on the non-illuminated face, for example from 3 to 5°C. Although our interest is in the simultaneous measurement of three diagonal components of α_o , equation 24 provides a way to (a) evaluate our experimental system and numerical methods for determining the 3-D components of $\alpha_o(C, T)$, and (b) determine a good initial guess for the nonlinear regression methods that will be needed to find the 3-D components (see below).

Measurement of thermal conductivity and specific heat

$K(C, T) = \rho_o c_F(C, T) \alpha_o(C, T)$ hence the thermal conductivity is easily found from the diffusivity, provided that the original density and the specific heat are known: for example, for the 1-D experiment just discussed, the out-of-plane thermal conductivity $K_{33} = (\alpha_o)_{33} \rho_o c_F$ where $\rho_o c_F = (Q/H T_M)$. Likewise, recall (from equation 16), that identification of a form of the free energy (and thus stress and entropy, equation 7) also requires that the specific heat be known. Hence, quantification of c_F as a function of finite strain and temperature is fundamental to a full thermomechanical constitutive formulation. The specific heat $c_F(I, T)$ is easily measured using differential scanning calorimetry (DSC), devices for which are commercially available. DSC compares the energy required to raise the temperature of a small (unloaded) specimen with the energy required to raise the temperature of a similarly sized specimen of a specific heat standard. Current DSC devices cannot be used to measure c_F as a function of finite strain, however, thus

² All prior solutions were for the spatial diffusivity α , where $\alpha = (F \cdot \alpha_o \cdot F^T)/J$, and thus one finds the same relation except that H is replaced with h (where $\lambda_3 = h/H$).

such data are apparently not available.

Consider, therefore, that the specific heat, $c_F = \partial \epsilon / \partial T$, is a scalar continuum property associated with either a unit volume or unit mass. In the absence of stress power, it can be estimated to be the ratio of the change in the total internal energy $\Delta \epsilon_T$ to the temperature rise ΔT , that is $c_F = \Delta \epsilon_T / m \Delta T$ where m is the mass of the sample. Yet, this equation, which forms the basis of DSC analysis, assumes a uniform temperature change throughout the specimen. This will not be true in general. Indeed, we wish to explore the possibility of determining the specific heat of a specimen, at various states of finite strain and temperature level, from a thin biaxial sample that is subjected to a nearly uniform burst of radiant energy. In such a case the temperature in the specimen will clearly be non-uniform in the in-plane dimensions; the out of plane dimension, being at most $1/30^{\text{th}}$ of those in-plane, will reach thermal equilibrium more quickly. Hence, consider a volumetrically averaged specific heat,

$$\bar{c}_F \approx \Delta \epsilon_T \left(\frac{m}{V} \sum_{i=1}^{\text{pixels}} \Delta T_i \Delta V_i \right)^{-1} \quad (25)$$

where "pixels" suggests that the temperature field on the entire non-illuminated face will be known (e.g., digitized from the output of an infrared camera). At present, however, this is only a preliminary idea; much work remains to determine the best way to determine $c_F(C, T)$.

A FEASIBILITY EXPERIMENT

In conjunction with our theoretical developments, we assembled a simple biaxial loading frame to test our hypothesis that the dependence of α_0 on C cannot be neglected in the elastomers of interest here. Constructed of 1.9 cm thick 303 stainless steel, the 17.8 x 17.8 cm loading frame (Figure 4) could be placed within a 30.5 cm diameter bell jar so that experiments could be performed under vacuum to evaluate possible effects of convection. Oil-impregnated bronze bushings guided orthogonally mounted pairs of stainless steel loading carriages, which in turn subjected square specimens to finite biaxial extensions via four arrays of loading strings. Specimens were loaded by hand by turning four bolts, and allowed to stress relax for 10 minutes. Associated extensions were measured using a hand caliper, but the loads were not measured -- we were only interested in determining the effects of finite strain on α_0 , not in constitutive formulations.

A flash system was developed (described below) and used to uniformly illuminate (via typically 50 J in 135 μ s) multiple silicone samples. Initial measurements of T on the non-illuminated face were accomplished using a "thermocouple probe". This probe consisted of two 0.254 mm diameter T-type (copper-constantan) thermocouples, each of which were inserted into a 0.794 mm diameter ceramic insulator. The probe was then mounted on a 1/4" x 20 stainless steel machine screw which allowed the thermocouples to be brought into contact with the specimen (with an unknown contact load) by advancing a screw. These small diameter thermocouples had a rapid response time ($O(0.05)$ s) in still air, but we switched to 0.51 mm diameter E-type (chromel-constantan) thermocouples which

have the highest Seebeck coefficient in the range of temperatures considered. This E-type probe was used to gather most of the initial data, and is still being used (albeit modified to hold three thermocouples). Temperatures were initially monitored using a Fluke Hydra model 2620-A; this unit is only capable of monitoring three thermocouples every 1.3 seconds, with an approximate uncertainty of 0.5°C . For 1.5 mm thick silicone specimens, the $t_{1/2}$ (equation 24) was about 4 seconds and T_M was about 3°C . Hence, this system did not have adequate temperature or time resolution. Next, an available Data Translation A/D board (DT 2805) was used (in a 386SX IBM compatible computer) to try to get better resolution. This system was capable of measuring three channels in 0.143 seconds, but only to within approximately 0.5°C . This system was, therefore, also inadequate. Nonetheless, associated pilot data collected in March 1995 revealed, as expected, that the out-of-plane diffusivity (calculated using equation 24) varied significantly with finite strain. Figure 5 shows a representative temperature rise on the non-illuminated face, and Figure 6 shows results for the out-of-plane diffusivity as a function of finite uniaxial strain. These pilot data, combined with aforementioned theoretical considerations, justified the design of a new system capable of determining multiaxial thermoelastic and thermophysical properties over a broad range of finite strains, temperatures, and environmental conditions. This system is described in detail below.

NUMERICAL SIMULATIONS

Finite element stress analysis

Equations 13-15 and 20 assume that the stress and strain fields are homogeneous, that is independent of position within the sample. In an actual experiment, however, there will be significant variations in both fields because of the necessity to load the samples with multiple point loads as seen in Figure 4 (this allows the specimen to deform freely in the direction orthogonal to the applied load). Though it has been shown empirically that strains are homogeneous within a central region of biaxially loaded samples (Treloar, 1948; Humphrey et al., 1990), and via finite elements for one class of elastomers (Nielson et al., 1991), we performed a finite element analysis to determine the extent of the central homogeneous field. Assuming a Mooney-Rivlin type hyperelastic behavior (i.e., $W = c_1(I_C - 3) + c_2(II_C - 3)$, where c_i are material constants and W is the strain energy), the ABAQUS[®] finite element code was used to study possible experimental configurations, that is the effect of the position and number of point loads. Because of double-symmetry, one-quarter of the specimen was studied; 1200 (i.e., $20 \times 20 \times 3$) hybrid brick elements were used to discretize the domain, which was taken to be 15 mm per side. Cases were run with even or odd numbers (4, 5, 6, 7 and 8) of equally spaced point loads per side. Figures 7a and 7b show results for an equibiaxial stretch of 10%. As expected, we found that at least 5 point loads were needed per side to ensure that the stress and strain fields within the central 25% of the overall area was homogeneous to within 3%.

Thermal diffusivity calculations

As mentioned above, determination of the three (diagonal) components of α_0 requires that the 3-D heat equation be solved for the temperature field $T(X,t)$ throughout a biaxially stretched specimen that is exposed to a burst of radiant energy over part of the "illuminated surface" (recall Figure 2b); indeed, multiple solutions are needed at various fixed C and various, constant ambient temperatures. Clearly, this solution must be achieved numerically, the accuracy of which depends primarily upon how well boundary conditions are approximated. It is usually assumed in the flash method that a uniform and instantaneous heat pulse is absorbed in a thin layer of a homogeneous, opaque, and insulated sample. In reality these conditions are seldom met, especially for samples of low to moderate thermal conductivity. In order to understand these problems, 2-D models have been used in which thermal diffusivity has been determined by temporal moments (Digiovanni and Laurent, 1986) or by use of Laplace transforms (Gembarovic and Taylor, 1993). Nonlinear regression schemes have also been used extensively (Gembarovic et al., 1990; Vozar et al., 1991; Sawaf and Ozisik, 1995). For example, Sramkova and Log (1995) used the Marquardt-Levenberg estimation scheme in combination with a model that accounted for heat loss. They provided a comparison of results from other authors techniques using NIST standard materials, and claimed excellent results.

Our approach has been to combine the Marquardt regression method with a finite difference solution of the heat equation. In particular, the heat equation is solved using central-differencing in space and explicit first order differencing in time. An explicit method offers several advantages over an implicit method. For example, the implicit model requires simultaneous solution of all nodal temperatures at each time step -- this requires inverting a large matrix at each time, thus this method is time consuming when the number of discrete time points is large. In contrast, an explicit method calculates present time directly from past time; because the solution marches forward in time, it does not require as much computational time to calculate temperatures at each discrete time. One-, two-, and three-dimensional codes have been written in FORTRAN to analyze modified flash experiments. Before discussing results from our preliminary simulations, however, first consider the parameter estimation method.

The Marquardt-Levenberg algorithm has been shown to be robust for determining elastic parameters from biaxial stretching tests on rubber (Twizell and Ogden, 1983) and tissues (Humphrey et al., 1990), as well as thermal conductivities in solids (Sawaf and Ozisik, 1995). Briefly, this algorithm is a nonlinear least-squares method wherein one seeks to minimize the objective function e ,

$$e = \sum_{k=1}^{n_m} (y_t(p) - y_e)_k^2 \quad (26)$$

where n_m is the total number of measurements (i.e., number of measurement sites times the number of data points at each site), y_t the vector of theoretically determined values (e.g., stresses or temperatures), p the vector of material parameters (e.g., material moduli or diffusivities), and y_e the vector of experimentally determined values. Values of p are found iteratively, via

$$(J^T J + vI)(p^{(i+1)} - p^{(i)}) = -J(y_t - y_e)^{(i)}, \quad J = \left(\frac{\partial y_t}{\partial p} \right)^{(i)}, \quad (27)$$

where i is an iteration counter and v the Marquardt parameter; v is typically initialized to ~ 0.01 , and multiplied or divided by 10 if e increased or decreased during the prior iteration. Iterations continue until a norm of the difference between the $p^{(i+1)}$ and $p^{(i)}$ vectors becomes less than a prescribed value. We have extensive experience with multivariate, constrained regressions using the Marquardt method (e.g., see Humphrey et al., 1990).

To determine the three diagonal components of the thermal diffusivity, we must minimize the difference between the temperatures measured and calculated at three different locations on the non-illuminated face of a specimen (see Figures 8a and 8b) at multiple times (i.e., not just at $t_{1/2}$ as in the 1-D problem, equation 24). Furthermore, the Marquardt regression must be initialized by providing initial guesses for the values of each of the parameters, that is $p^{(1)}$; it is well known that the Marquardt method is relatively insensitive to the initial guess, but certainly the better the guess the more reliable and faster the regression. In practice, good initial guesses can be obtained by using equation 24 and a uniform flash to determine the out-of-plane component, and then using this value as a guess for all three components in a full regression, given the same biaxial strain state and ambient temperature. Best-fit values for each state can then be used as initial guesses for subsequent states (i.e., strain and temperature level).

Before evaluating the combined Marquardt-Finite Difference code, however, we first verified that the finite difference solution was reasonable. For example, we used a 2-D model to evaluate the uniform flash experiment for which a 1-D solution (equation 24) is available. The "specimen" was taken to be $10 \times 10 \times 0.1$ cm, and assumed to be silicone rubber (HSII) having an isotropic thermal conductivity α of $0.22 \text{ W/m}^2\text{K}$. The specimen was exposed to 50 J of energy with a flash time of $100 \mu\text{s}$. Figure 9 shows the non-illuminated face temperature as a function of the position from the centerline of the sample; temperature was non-dimensionalized as

$$\Phi = \frac{T - \bar{T}_o}{\Delta \bar{T}}, \quad \Delta \bar{T} = \frac{q_a}{\rho_o V C_F} \quad (28)$$

where q_a is the absorbed energy, V the specimen volume, and the overbar denotes a volumetric average. As can be seen from Figure 9, $>95\%$ of the non-illuminated face of the sample achieved a uniform temperature (after $4t_{1/2}$) that was $>90\%$ of T_M . That is, losses at the edge of the sample were not significant within the observation period of interest, and therefore the 1-D solution is appropriate. A 1-D explicit finite-difference model for the uniform flash method, including convection effects, is currently being compared to the analytic 1-D solution for further validation of the numerical solution. Nonetheless, the importance of numerical simulations is evident: this study revealed that uniform flash experiments are tractable for homogeneous rectangular elastomeric

specimens, and convection losses are minimal even when the experiments are performed in air rather than in a vacuum.

A 3-D explicit Cartesian finite-difference model was then developed to study the non-uniform illumination experiment: that is, illumination of a square specimen through a smaller square aperture as seen in Figure 8a (recall from Figure 2b that Malliet et al. (1990) used a circular aperture and a square specimen). Figure 10 reveals the model and boundary conditions: the aperture size was 6.5 x 6.5 mm and the specimen size was 30 x 30 mm, but symmetry allowed examination of only one quadrant. The boundary conditions were (a) insulated centerline edges, (b) natural convection on the outer edges and non-illuminated face, and (c) a step from a constant heat flux to a convective boundary on the illuminated face. Figure 11a shows representative temperature histories at different positions on the X_2 axis of the specimen. This model revealed locations for thermocouples on actual specimens that will yield a measurable temperature rise in the in-plane directions. Figure 11b reveals further, however, that the temperatures calculated in the in-plane directions exhibited a strong nodal dependence, likely due to steep temperature gradients at the boundary of the illuminated region. For example, there was a 3.7°C change in the in-plane directions in comparison to a 0.1°C change in the out-of-plane direction over the same difference in nodes (i.e., 10 and 100 nodes). Hence, the mesh must be chosen carefully to ensure reliable parameter estimation.

Given that the finite difference model gave reasonable results, we then performed a sensitivity study to evaluate the robustness of the combined Marquardt-Finite Difference code. Briefly, we prescribed values of the diffusivity and specimen dimensions, and used the finite difference algorithm to solve the temperature field associated with a prescribed "flash". Values at three locations on the non-illuminated face, that is $T(X_1, X_2, H, t)$, were then perturbed by adding random Gaussian noise (to simulate experimental errors) and used as input to our Marquardt regression as experimental data. In this way, we could evaluate the robustness of our algorithm as a function of the location of the temperature measurements, number of data points, amount of experimental noise, goodness of our initial guess, etc. As expected, the combined Marquardt-Finite Difference parameter estimation worked well for the 1-D model (for which needs to determine only one parameter). Nonetheless, we are now comparing the finite difference and analytical based (equation 24) regressions for speed and accuracy. The results from these tests will further support the use of the numerical model in our experimental data reduction. Likewise, the 3-D explicit finite difference model was incorporated into a multivariate Marquardt parameter estimation scheme to determine the three diagonal components of α_0 . Initial evaluation of this code, using numerically generated "data" without noise, revealed that we could recover known parameters to within 0.1% in less than 10 iterations. As expected, convergence was quicker in the out-of-plane direction than in the in-plane directions. This is due to less overall sensitivity of the thermal diffusivity in the out-of-plane direction, thus thermocouple location and aperture alignment have a substantial effect on the determination of in-plane thermal diffusivities. Additional, more complete estimations are currently

in progress.

EXPERIMENTAL SYSTEM

Figure 12 is a schema of the overall optical-thermomechanical system. Briefly, the system consists of six sub-systems, that is one each for (a) biaxial loading, (b) in-plane biaxial strain measurement, (c) thickness measurement, (d) ambient temperature control, (e) flash illumination, and (f) point-wise temperature measurement. Each sub-system is discussed in order below.

Biaxial loading

Oblique and top views of the device are shown in Figures 13a and 13b. The loading frame (LF) is constructed from one piece of mild steel having overall dimensions of 45.72 x 45.72 x 2.54 cm, and a 2.54 x 2.54 cm cross section. The frame is mounted, at each corner, on an optical table using four standard 2.54 cm diameter, 15.24 cm long optical rods to ensure stability (Figure 13a). All surfaces in the plane of the frame are ground so as to ensure flat and parallel faces for mounting the various components that make up the loading frame. Pairs of through holes (1.27 cm diameter and 4.445 cm apart) house recirculating bearings (1.905 cm long) on each side of the frame. These bearings allow linear travel, with minimal play, of four pairs of 0.635 cm diameter solid steel loading shafts, which form two opposing sets of load carriages (CAR). Each shaft is also supported by a rulon bearing that forms a watertight seal within the wall of the environmental chamber (EC). Proper alignment of the environmental chamber and loading frame ensure minimal sticking and thus smooth translation of the load carriages.

The inside half of the load carriage consists of four separate parts (Figure 14), all made of stainless steel. The first part is a cross bar that serves to hold the two shafts in place as well as holding a load cell (LC) or a spacer rod. The load cells are easily interchangeable, but are currently 9.8 N Sensotec transducers that are temperature compensated (over the range -20F to 200 F) and shielded against wet environments. These cells will be used during tests on natural rubber, whereas 445 N load cells will be used for tests on other polymers, such as polyurethane. The load cells are excited by a signal conditioner/amplifier (SA-4), which in turn is connected to a 12 bit A/D board for load registration. Mechanically attached to the load cells and spacer rods is a coupling bar which holds an interchangeable T-section. This T has a series of equally spaced holes (e.g., 7.5 mm apart) which will serve as rigging points for the arrays of Kevlar[®] (MIL-T-87128) threads (K) that attach to the specimen (S). On the other end of the shafts is a similar cross bar that holds the shafts in a similar fashion, and facilitates load application.

Currently, the load is applied by hand using a threaded rod. That is, a 15.24 cm long 1/2"-13 threaded rod is attached to a face plate that is mounted directly on the outer surface of the load frame. The rod passes through a 1.27 diameter hole in the outside crossbar. Linear translation of the load carriage is achieved by manually rotating a nut on the inside of the crossbar in either

direction. Although this system is sufficient for many of our envisioned tests (which require both thermal and mechanical equilibrium), we are in the process of converting to micro-stepper motor control. Four independently controlled motors (M) will drive the loading rods via a ball screw and ball nut (attached to the cross bar). The motors will be attached to the ball screw using flexible couplings, and supported from the tabletop via a bracket (SUP). By using two pairs of oppositely moving loading frames, the center of the specimen will remain fixed, which in turn facilitates strain measurement. The four motors will be controlled individually via a four axis indexer and controller residing in a PC; we have considerable experience with similar devices (e.g., see Humphrey et al., 1993).

Biaxial strain measurement

Because of the homogeneity in the central region of the specimen, in-plane strains (extension and shear) are easily calculated from the motions of 3 to 4 surface markers. We have used this technique extensively before, which is described elsewhere (Humphrey et al., 1990; Downs et al., 1990). Briefly, however, note that four small white markers will be affixed to the central region of the specimen on the face that will be illuminated during a flash (recall Figure 8b) -- the specimen will be darkened in order to improve the absorption of radiant energy, thus white markers will contrast well against the dark background and thereby be easily tracked. Note, too, that strains will be measured continuously during thermoelastic tests (in the absence of a flash) and at mechanical and thermal equilibrium prior to a flash. Hence there will be no interference between the flash and video-based strain measurement. Having the strain and flash systems focus on the same face also leaves the non-illuminated face (actually the space above it) free for the thermocouple probe. Nonetheless, the centroids of the markers will be tracked on-line at the 30 Hz frame rate using custom correlation-based software (Downs et al., 1990). Given the marker positions, one can use interpolation functions (e.g., bilinear) to construct continuous displacement fields within the central region, which in turn can be used to calculate the displacement gradient tensor H . Since $F=I+H$, the deformation gradient can thereby be determined, and hence all necessary measures of strain.

The marker motions will be monitored with a CCD-Iris camera (Sony SSC-M370) via an optical mirror (mounted directly beneath the specimen, and at 45° to the optical table); the CCD and reflecting mirror are denoted by C and R, respectively, in Figure 13b. The CCD has a 1.27 cm² chip area, and its output is fed directly into a DT 2853 video frame grabber board as well as a B&W (Panasonic TR-990C) monitor (Figure 12). The frame grabber digitizes the image in real time, thereby allowing the correlation algorithm to determine the marker locations. Currently, we are using a Canon 100 mm f4 macro lens, which has a magnification of 0.5 at its focal length. A C-mount adaptor couples the lens to the CCD.

Thickness measurement

Although the mechanically-induced deformations are nearly isochoric (i.e., $\lambda_3 = 1/\lambda_1\lambda_2$; see equation 12 and the related discussion), the thermally induced deformations are not (recall Figure 1 and that $F_1 = \Delta I$). Hence, the current thickness h of the specimen must be measured as temperature changes. We have investigated several options for on-line thickness measurement, but we have yet to find a satisfactory method. One option, however, which is the simplest in principle, is to recall that $\det F = \Lambda^3 = \rho_0/\rho$, where the current mass density ρ will change with temperature -- volume changes are on the order of 10^{-4} per degree C. Hence, by simply measuring $\rho(T)$, the temperature-induced thickness changes can be calculated. This is being explored.

Environmental chamber and ambient temperature control

As mentioned above, we seek to measure thermoelastic and thermophysical properties at (ambient) temperatures levels over the range $T \in [20, 100^\circ\text{C}]$, and under a variety of environmental conditions (e.g., humidity, solvents, etc.). This requires a closed environmental chamber and active temperature control. The chamber (EC in Figure 13) is a layered sandwich structure constructed of a thin inner layer of silicone rubber (to prevent leakage), a central layer of polycarbonate (for stiffness), and an outer layer of polystyrene for insulation against parasitic heat losses due to conduction and radiation. Specifically, the 1.27 cm thick central polycarbonate shell is 40 x 40 x 7.62 cm in outer dimension, and thus fits snugly on the inside of the load frame. A pair of holes on each side of the chamber allow the loading rods to pass through to the inside. These holes are fitted with neoprene rubber seals, consisting of a rulon bearing and an o-ring at each end of the bearing; this minimizes any leakage, and reduces heat loss (except due to conduction along the rods).

Two face plates, one on the top and one on the bottom, are attached to the shell using 8 nylon bolts each; 0.16 cm thick silicone gaskets prevent heat loss and fluid leakage from the chamber. Note, too, that each face plate is designed differently. The bottom plate (Figure 13a) contains a centrally mounted, thin quartz window through which the specimen can be heated using the flash system (see below) or monitored using the video-based strain measurement sub-system. The quartz window is raised relative to majority of the surface of this face plate, and thus is 1.27 to 1.905 cm from the bottom surface of the specimen. This allows the flash lamp to be placed closer to the specimen, which in turn improves heat transfer. The bottom face plate also has two drainage ports to remove fluid from the chamber when needed - recall that some thermoelastic tests will be performed with the specimen immersed. Adequate space is provided under this face plate for both an optical mirror (for the strain measurement system) that is mounted on the optical table, and the flash system which is mounted to the plate (F in Figure 14). The top face plate is much simpler. Besides the necessary access ports for wiring etc., the only other feature is an 2.54 cm diameter central hole which allows the thermocouple probe to contact the central region of the non-illuminated face at select locations on the top surface of the specimen (recall Figure 8).

Prior to the final design, the heat loss from the chamber was estimated for the maximum expected ambient $T = 100^{\circ}\text{C}$. This was done by taking into account the quartz windows and access port for the thermocouple probe as well as conduction and radiation losses through the walls and the support rods of the carriages. The total loss was calculated (using 1-D resistance models for the walls) to be approximately 700 W. As expected, the estimated heat loss from the walls of the chamber and the support rods of the load carriages was 1/10 that through the windows which are not covered with the 2.54 cm thick polystyrene. Hence, to maintain ambient equilibrium temperatures up to 100°C , and some symmetry in the heating, power is to be supplied by a pair of immersible rod heaters (H) that fit within the confines of the chamber (Figure 13). These rods (Omega) are 1.27 cm in diameter and 30.5 cm long, and require a maximum of 120 VAC; each is capable of supplying 750 W. Initially, the voltage supply was supervised manually using a voltage regulator. Thermal control was good, but not adequate for precise measurements. Consequently, we are currently evaluating a controller (Cole Parmer 2186-20A) which responds to feedback from a thermistor; this will require one more probe in the experimental chamber, but potential improvements in the control of the chamber temperature warrant this change. Similar control is expected for a fluid-filled chamber.

Flash system

In essence, a flash system consists of a source of radiant energy such as a lamp, possibly an aperture plate, a specimen, and a temperature measurement system on the non-illuminated side of the sample. Here we discuss the energy source. We selected an EG&G linear xenon flash tube (0.4 cm diameter and 11.5 cm long) which is rated to deliver a 240 J explosion energy at a pulse duration of $< 135 \mu\text{s}$. The custom circuit for the lamp source is shown in Figure 15; note that the 136 μF capacitance is actually built up using a series of smaller capacitors. The calculated energy output from this circuit is 80 J based on a 1000 Amp input current. The operation of the lamp is straightforward. In the non-ionized state, the flash tube has a high impedance, which causes the current from the power supply to flow into the charging capacitor. The instant the trigger is released, the voltage across the tube increases and xenon atoms within the tube ionize. This causes a rapid drop in the impedance of the tube. In a very short period, enough atoms are ionized to allow the current to flow from the capacitor through the flash tube. As this continues, an arc expands to fill the tube. However, in a short period most of the current from the capacitor is released, and the atoms deionize and stop conducting. This allows the capacitor to recharge.

To better focus the energy from the lamp (which is emitted radially) onto the specimen, a linear cylindrical mirror is placed behind the lamp (Figure 14) and the surface of the specimen is darkened with carbon black or India ink. As mentioned above, the specimen is also illuminated through a square aperture (recall Figure 8a) in order to heat only a portion of the surface -- this allows the in-plane components of the thermal diffusivity to be determined. The aperture will be mounted within the device in order to place it as close to the specimen surface as possible. Thus,

although the total energy from the lamp can be calculated, that portion which reaches the sample must be determined by placing an instrumented (with thermocouples) blackened, high conductivity metallic plate of known mass and specific heat just in front of the specimen and discharging the lamp; the high conductivity ensures nearly uniform heating. The energy absorbed is found via $Q = \Delta \epsilon = c_p m \Delta T$ (recall equation 25).

Temperature measurement

Two sets of temperatures must be measured on-line: the ambient temperature in the central region of the chamber, and the temperature at three orthogonal locations on the non-illuminated surface of the specimen (Figure 8). For reasons of cost effectiveness and general utility, thermocouples are currently being used (below we document design considerations based on possible IR camera measurements). The ambient temperature is easily measured with a T-type thermocouple. In contrast to the pilot studies mentioned above, the surface temperature is measured at three orthogonal locations (Figure 8) using E-Type thermocouples that have response times of < 0.05 s, a nominal bead size of the order of 0.033 cm, and a wire diameter of about 0.0254 cm. These three thermocouples are each placed in a 0.035 diameter, 2.54 cm long glass tube (to provide stability, insulation, and electrical isolation), which in turn is mounted in a 1.905 cm Delrin disk. Mounted in this way, the thermocouples form an equilateral triangle of 4.5 mm per side; this corresponds to a length slightly larger than the size of the current aperture through which the specimen is illuminated. The center thermocouple is placed at the center of the specimen, which coincides with the center of the illumination region, in order to measure the out-of-plane diffusivity whereas the other two measure the in-plane diffusivities. The Delrin disk is mounted on a moveable aluminum bracket, which allows the three thermocouple beads to be simultaneously brought into contact with the surface (with the appropriate alignment). The placement of the probe is accomplished via a micrometer. Because the surface temperatures will be measured at multiple states of finite strain (each at mechanical equilibrium), there is a need to re-adjust the position of the probe for each strain state. Moreover, because the temperature measurement is a function of the contact force (i.e., contact conductance), a calibrated spring will be mounted on the probe to allow repositioning at a fixed, prescribed indentation load.

Although not currently used, we evaluated the potential advantages of infrared temperature measurement, that is IR cameras. IR cameras measure entire temperature fields $T(\mathbf{x}, t)$, and thus may be used to estimate the specific heat (recall equation 25) as well as provide data needed for a Marquardt-based determination of the components of α_0 (equation 27). The decision to use IR cameras is not a trivial one, however, as we shall show.

It is well known that all matter warmer than 0 K emits electromagnetic radiation. An ideal emitter, or black-body, will have a spectral emission described by Planck's distribution, with a total emissive power proportional to T^4 . Thus, one can determine the temperature of an object by measuring the power emitted from

it. Wien's Displacement Law further states that the wavelength of maximum spectral emission is related to temperature by $\lambda_{\max} T = 2897.6 \text{ K}\mu\text{m}$, where λ_{\max} is the wavelength at the maximum emissive power and T is the absolute temperature of the surface. For example, the temperature during heat-treatment of metals is often estimated by the specimen color: for example, $\lambda_{\max} = 9.9, 7.8$ and $0.5 \mu\text{m}$ for $T = 293.2, 373.2$, and 5800 K , respectively. Disadvantages, however, are that IR temperature measurement is expensive, inaccuracies arise if the emissivity of the surface is unknown, and the response time for full field interrogation needs improvement. Furthermore, measurements cannot be made through a medium which absorbs IR radiation, such as water. Yet, IR cameras remains an active area of R&D -- size, minimum discernible temperature (MDT), and scanning rate are constantly being improved -- and the desire to measure $c_F(C, T)$ suggests that they must be considered as a candidate system. Table 1 contains information on the commercially available cameras considered in the summer of 1995. Of these, the Cincinnati Electronics and AGEMA models were examined in our laboratory using the prototype load-frame and flash system (recall Figure 4). Results suggested that before these cameras could be used to their full potential (a) optional lenses would be needed, and (b) a method of accurately digitizing the full-field signal would need to be developed. The optional lenses available for long distance imaging are typically between \$20 and 30k; IR lens are much more expensive than standard lens since they are made in much smaller quantities. Video boards with enough speed and buffer memory to record data in real time and with adequate resolution were about \$ 5k. Hence, it appears that independent of unresolved technical disadvantages, an entry level IR system would cost > \$ 90k, which was well above our equipment budget.

Consequently, we then evaluated the possibility of designing a custom temperature measurement system using discrete IR detectors (as compared to the 128×128 or 256×256 arrays of typical IR cameras). That is, three IR detectors could be used in an array, and thereby provide information similar to that given by the thermocouple probe. Given the expected temperature range in our studies (and hence the peak emissive power wavelengths), we found that Mercury-Cadmium-Telluride (MCT) and Mercury-Manganese-Telluride (MMT) sensors have the highest D^* ($\sim 10^{11} \text{ cmHz}^{0.5} \text{ W}^{-1}$), a scaled measure of the IR sensitivity of the detectors. Vendors that were contacted were Electro-Optical Systems (Phoenixville, PA), Brimrose Corporation of America (Baltimore, MD), and EG&G Judson Optoelectronics. Brimrose (MMT) and Electro-Optical Systems (MCT) were willing to develop unique detectors with the characteristic dimensions needed for the measurements, average costs of which were quoted to be about \$10 k. EG&G was not willing to develop unique sensors at a competitive cost. The draw-backs of the discrete sensors, however, are (a) the need to design and develop unique IR optics, (b) the lack of a priori knowledge of their thermal sensitivity and calibration, and (c) cost. Electro-Optical Systems, for example, suggested purchasing a single sensor at \$2k to test its applicability. This, in turn, would have required purchasing IR optics, estimated at \$5k (including optical mounts). A > \$7 k expenditure to evaluate a sensor was not justifiable.

Nonetheless, a design of the requisite optics was developed.

As with visible optics, there are both transmission and reflective IR optics. Transmission IR optics follow the same principles as optics used in the visible spectrum, but require exotic materials such as germanium (Ge) and zinc selenide (ZnSe). These materials have physical properties that make them generally difficult to machine and use; Ge, for example, is opaque to visible light, which makes alignment difficult. An advantage in fabrication, however, is the long wavelength in the IR spectrum -- optical tolerances are often quoted in terms of fractions of a wavelength, usually the wavelength in the center of the spectrum of interest; for example, a quarter wavelength tolerance for a HeNe laser at 632 nm requires more precise machining than for an IR component at 10 μm . Optical design³ was led by Dr. Henry Cox, a retired optical designer from Annapolis MD, who donated his time to the project. His proposed design (Figure 16) consists of two parabolic mirrors, with focal lengths of 240 and 300 mm, respectively. The mirrors were to be machined from 6061-T6 aluminum alloy, and the optical faces gold plated. Accurate manufacture of the optical elements is critical. Quotes for the mirrors were obtained from Janos Technology (\$3 k) and the Center for Applied Optics at the University of Alabama at Huntsville (\$ 2.8 k). Material to support the mirrors would be machined at UMBC.

In summary, the expense, uncertainty, and need to measure temperatures on submerged specimens led to the use of E-type thermocouples. Nonetheless, the potential advantages of having the entire temperature field on the non-illuminated face remains attractive, and IR measurement techniques will continue to be evaluated as the technology improves.

Data Acquisition and Control

The description of the primary sub-systems and theoretical framework highlights the need for adequate acquisition of the required data. Depending on the particular test protocol employed, as many as 6 independent channels of information will need to be recorded via the A/D board (two forces, and four temperatures) and 4 surface markers will have to be tracked using the video system (i.e., 4 (x_1, x_2) pairs). Of course, the strain and diffusivity related temperatures need not be measured simultaneously. Similar to the signal conditioner/amplifiers for the force transducers (SA-4 card), separate amplifiers (Omega OmniAmp III) were purchased to amplify the thermocouple signals 1000 fold. Amplification improved the signal to noise ratio considerably. Specifically, the load and temperature signals are read, via a DT707 external jumper board, by a standard 12 bit A/D board (DT 2837); this board is specifically designed for acquisition of thermocouple data and thus is equipped with a cold junction compensation circuit at the 0 channel. The thermocouples occupy channels 1-4, and the two load cells channels positions 5 & 6, respectively. The computer platform is a 90 MHz Compaq Pentium personal computer, and a custom program allows one to vary the sampling rate and gain per channel independently.

³ See Modern Optical Engineering by W. Smith (McGraw-Hill, 1990).

A serious problem in the development of the system was that of unwanted electrical noise. In particular, this problem became acute when measuring thermal diffusivities in thicker specimens wherein the temperature rise on the non-illuminated surface was low (i.e., $<1^{\circ}\text{C}$). At sampling rates above 50 Hz, for example, the signal to noise ratio was low even at peak gains of 500 for the data acquisition board. The reasons for this are varied, but the flash tube alone causes currents of the order of 1000 Amps and voltages of about 16000 V (and thus significant electromagnetic radiation). Fortunately, electrical isolation has largely been achieved.

Pilot tests

Two types of materials have been tested: natural gum rubber (NGR) and room temperature vulcanized silicone (HSII-RTV). NGR specimens were obtained in precast sheets with an initial thickness of 1.588 mm, whereas HSII RTV were cast and cured on site. For the latter, appropriate portions of the resin and hardener were mixed and poured into a polycarbonate cast; care was taken to ensure the removal of air within the mixture by placing the mold in a vacuum chamber; the mold was then set aside to cure for 24 hrs at room temperature. Square samples, measuring between 30-35 mm on a side, of each material were cut from the sheets. Test samples were then prepared by mounting in the following fashion. Approximately 2.5 mm away from each edge of the square sample a series of holes were punched out using a syringe needle (diameter 0.254 mm). Five holes were punched out on each side, approximately 5-6 mm apart. The sample was then mounted in the test frame by threads from each load carriage through the T-section mentioned earlier. A schema of the mounted sample appears as in Figure 14. All non-used samples were stored in a glass bell jar that is moisture-free and protected from visible light. This ensured virtually no contamination of the remaining samples.

Specific heats of the NGR, in the unloaded configuration ($F=I$), were determined using standard DSC over the range of temperatures between 25 and 85°C . The results of these measurements are shown in Figure 17, which reveal a nearly linear dependence of the specific heat with temperature. Pilot studies to determine the strain dependence of the three components of the diffusivity were performed in October of 1995 (even though the experimental system was not yet complete). The 3-D finite difference - Marquardt method was used to reduce the data. As expected from the aforementioned simulations, the thermal diffusivity in the out-of-plane direction converged quickly, but the diffusivities in the in-plane directions were far from the expected values. As can be seen from Figure 18, the temperature versus time data (on the non-illuminated face) for the transverse directions have similar curves for diffusivities of 16.7 and 7.0×10^{-8} for the first five seconds following the flash. These curves have vastly different shapes and values if examined for 10 seconds, however, thus it was found that the Marquardt estimation should be performed with data collected over longer times than those used ($t_{1/2}$) in the uniform flash studies. Moreover, the accuracy of the Marquardt parameter estimation was (as expected from the simulations) highly sensitive to the number of nodes in the finite difference model. Of course, as the number of nodes

increases the computational time for each iteration also increases. For example a model using $21 \times 21 \times 9$ nodes takes approximately 20 seconds per iteration on a Sun SparcStation5, whereas a $61 \times 61 \times 9$ node model takes 20 minutes per iteration. Thus when the number of iterations are as high as 50 (for noisy data) it takes significant time to reduce the data. Consequently, we are currently developing models that have a higher concentration of nodes where needed (i.e., in regions of steep temperature gradients), but fewer nodes overall. The governing equations must be transformed so that we may relate the nodal position as a given function.

CONCLUSIONS

Originally we proposed to use an existing experimental device to perform "standard" tension-torsion thermoelastic tests (e.g., see Treloar, 1975) on a number of elastomers and fiber-reinforced elastomeric composites. That is, the emphasis was proposed to be on data collection and constitutive formulations for a specific set of materials. Based on early discussions with ARL-MD personnel, however, it became clear that the focus should be changed to the design of a new experimental device for performing tests on small samples of candidate materials as they become available. Hence, we have designed a theoretically-motivated multiaxial test system that is capable of collecting thermoelastic and thermophysical data on small, thin sheets of elastomers that are subjected to a variety of finite strains, temperature levels, and environmental conditions. We submit that this device represents a significant advance in elastomer testing, and it will allow cutting-edge thermomechanical constitutive relations to be rigorously formulated. Many different design options were evaluated, theoretical concepts were developed, and numerical simulations were used to identify preferred tests. The device and much of the associated control and data reduction software is now complete.

REFERENCES

- Burland D, Shattuck & J Perrin (1989) J Imag Tech 15: 257-262.
- Anthony RL, RH Caston & E Guth (1942) J Phys Chem 46:826-840.
- Carslaw HS & JC Jaeger (1959) Conduction of Heat in Solids, Oxford Univ Press.
- Chadwick P (1974) Phil Trans Roy Soc 276: 371-403.
- Chadwick P & Creasy (1984) J Mech Phys Sol 32: 337-357.
- Coleman BD & Gurtin ME (1967) J Chem Phys 47:597-613.
- Dashora P (1994) Physica Scripta 49: 611-614.
- Dillon OW (1962) J Mech Phys Sol 10: 123-131.
- Degiovanni A (1977) Rev Gen Therm Fr 185: 420-442
- Downs J, HR Halperin, JD Humphrey & FCP Yin (1990) IEEE Trans BME 37:903-907.
- Gembarovic J & RE Taylor (1993) Int J Thermophysics 14:297-311.
- Gembarovic J & RE Taylor (1994) Rev Sci Instrum 65: 3535-3539.
- Gough J (1803) Mem Lit Phil Soc Manchester 1: 288-295.
- Humphrey JD, RK Strumpf & FCP Yin (1990) ASME J Biomech Engr, 112:333-346.
- Humphrey JD, T Kang, P Sakarda & M Anjanappa (1993) Annls BME 21:33-43.

- Humphrey JD (1995) J Elast (submitted)
- Joule JP (1859) Phil Soc R Soc Lond 149: 91-131.
- Kelvin Lord (ie, W Thomsom) (1857) A J Math 1:57-77.
- Lachi M & A Degiovanni (1991) J de Physique III, 12: 2027-2046
- Maillet D, M Lachi & A Degiovanni (1990) Thermal Conductivity 21, (CJ Cremers & HA Fine, eds), Plenum Press.
- Mark JE (1982) Rubb Chem Tech 55: 1123-1136.
- Mueller I (1985) Thermodynamics, Boston: Pitman.
- Nielsen PMF, PJ Hunter & BH Smaill (1991) J Biomech Engr 113:295-300.
- Ogden RW (1992) J Therm Stress 15:533-557.
- Parker WJ, RJ Jenkins, CP Butler & GL Abbott (1961) J Appl Phys 32: 1679-1684.
- Rivlin RS & DW Saunders (1951) Phil Trans R Soc Lond, A243:251-288.
- Sawaf B and N Oszisik (1995) Int Comm Heat and Mass Trans,
- Schapery RA and RE Martin (1974) J Heat Trans 225-231.
- Spencer AJM (1984) Cont Theory Mech Fibre-Reinf Compos, CISM Vol 282, NY: Springer.
- Sramkova T & T Log (1995) Int J Heat Mass Trans 38: 2885-2891.
- Treloar LRG (1976) The Physics of Rubber Elasticity, Oxford: Clarendon Press.
- Truesdell C & W Noll (1965) Handbuch der Physik III/3, Berlin: Springer.
- Twizwell EH and RW Ogden (1983) J Austral Math Soc 24B: 424-434.
- Vozer L, J Gembarovik & V Majernik (1991) High Temp High Pres 23: 397-402.
- Wood LA and GM Martin (1964) J Res NBS 68A: 259-268.
- Wright NT, M da Silva, DJ Doss & JD Humphrey (1995) Proceed 23 Int Conf Therm Cond., TN.

Table 1. IR cameras

company	model	sensor	cost (\$k)	MDT (K)	array size (pixels)	scan rate (Hz)
AMBER	Radiance 1	InSb	59	<0.025	256x256	60
C-E	IRRIS	InSb	80	<0.025	256x256	50-150
	IRC	InSb	30	<0.025	160x120	50
I-M	700 series	HgCdTe	60	<0.2@30Hz	256x200	7866
AGEMA	450	HgCdTe	27	0.1°C	100x140	30
	470	HgCdTe	80	0.1°C	100x140	30
	900	HgCdTe	140	<0.1°C	200x136	30
FSI	Prism	PtSi	32	0.1°C@30°C	320x244	60
	816	HgCdTe	80	0.05	348x240	30
ISI	VideoTherm	vidicon	21	0.15°C@25°C	272 lines	30

 C-E is Cincinnati Electronics

I-M is Infra-Metrics

FSI is FLIR Systems, Inc.

ISI is ISI Group, INC.

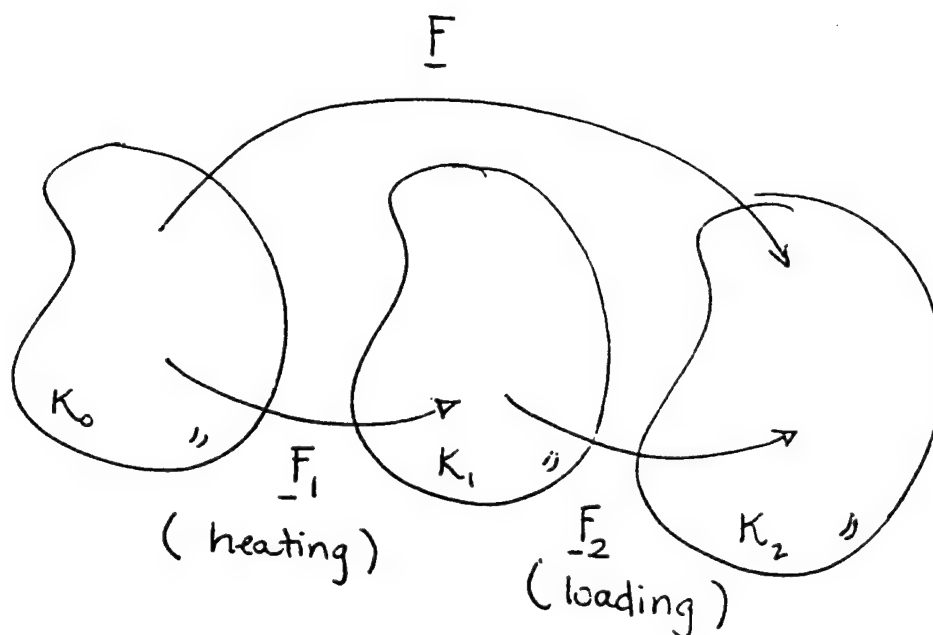


Figure 1. Schematic diagram of the decomposition of a thermoelastic deformation into that part due to heating alone (F_1) and that part due to isothermal stretching (F_2).

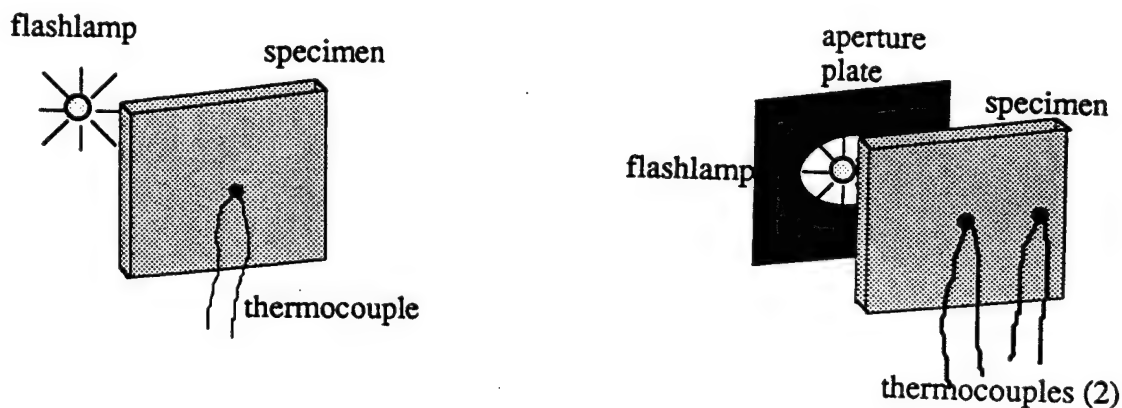


Figure 2. Schema of the uniform flash method proposed by Parker et al for measuring the out-of-plane diffusivity (panel a) and the modification of Malliet et al for measuring 2 components of α (b).

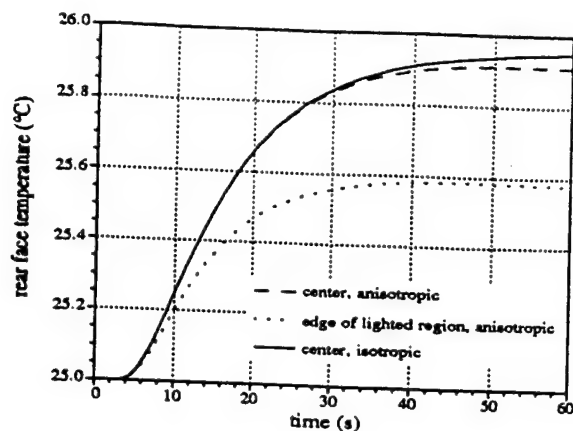


Figure 3. Simulations showing potential temperature histories on the non-illuminated face of stretched NGR sample.

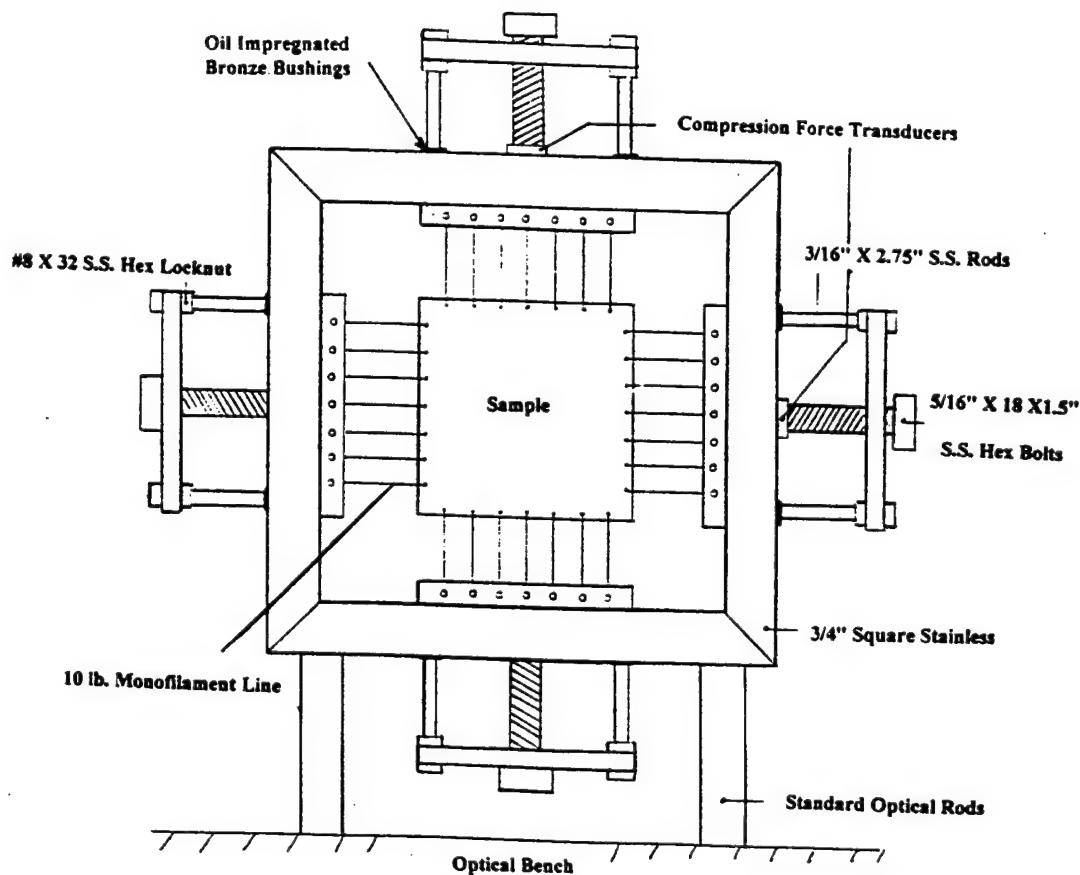


Figure 4. Preliminary biaxial load frame constructed to perform feasibility studies in the Spring of 1995.

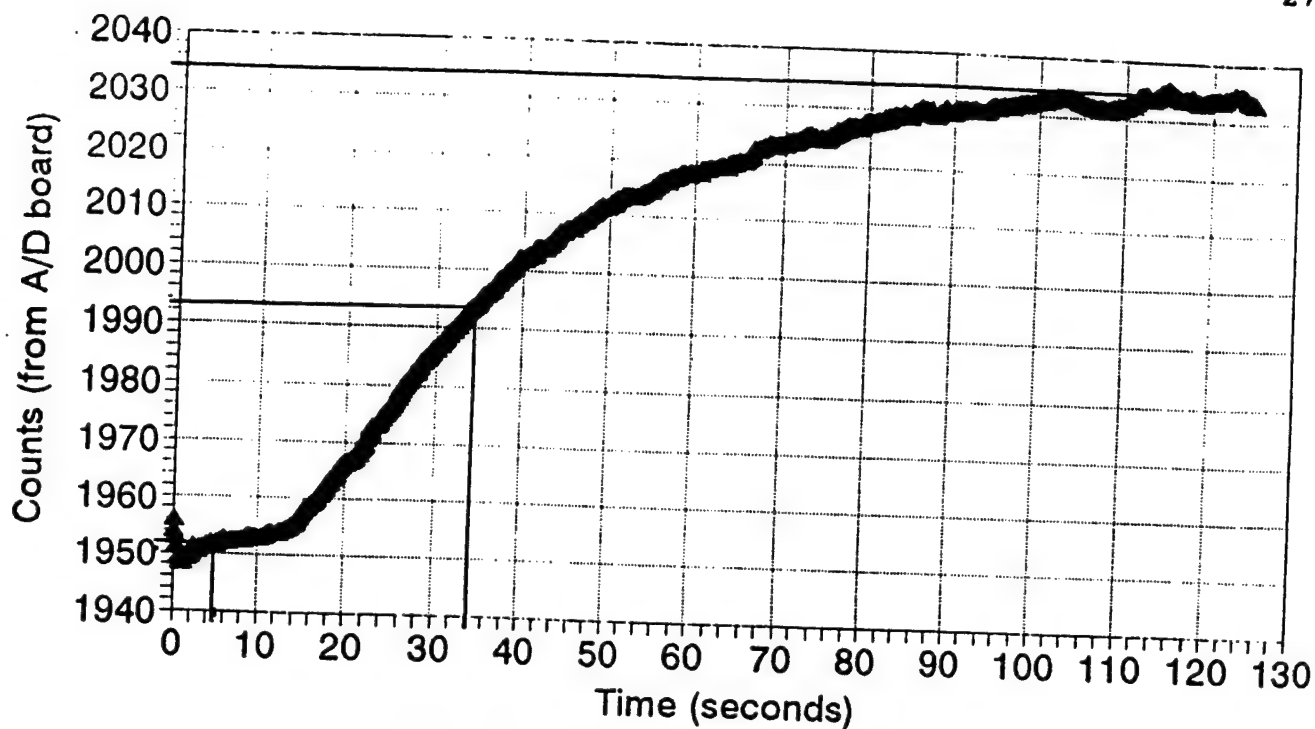


Figure 5. Pilot data on NGR: temperature history on the non-illuminated face of a uniformly flashed sample.

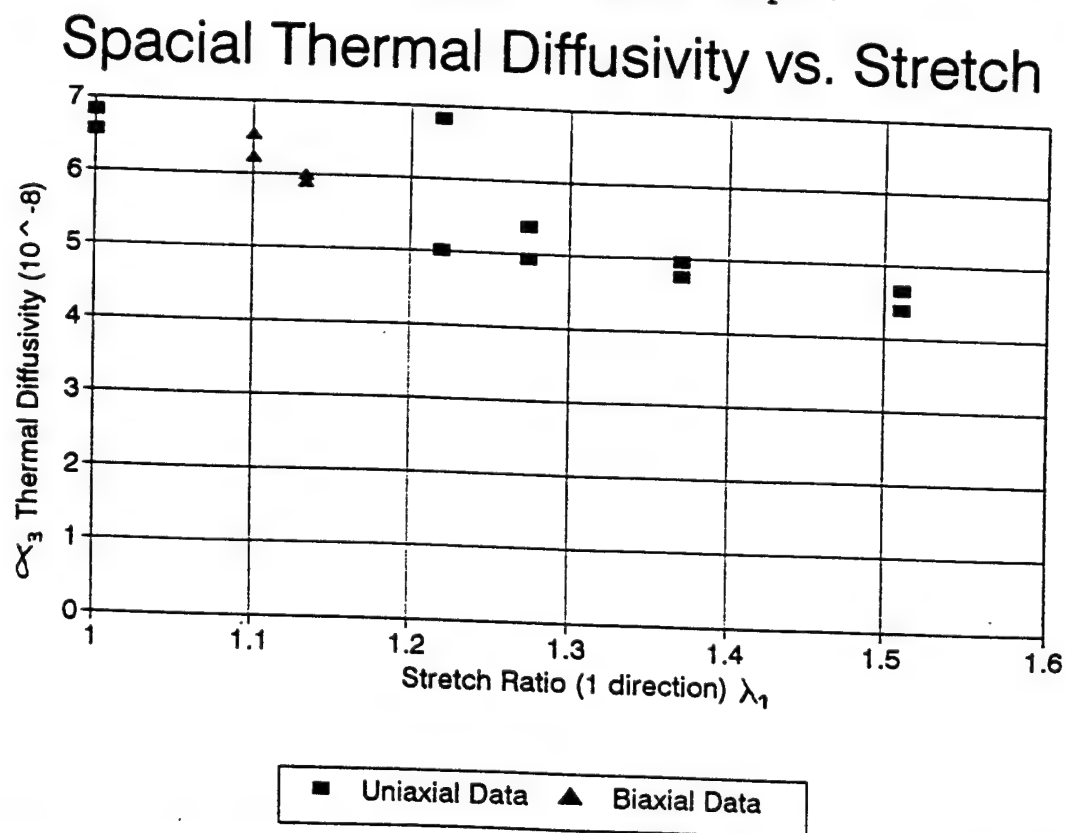


Figure 6. Pilot data on NGR: variation of the measured out-of-plane diffusivity as a function of finite uniaxial strain.

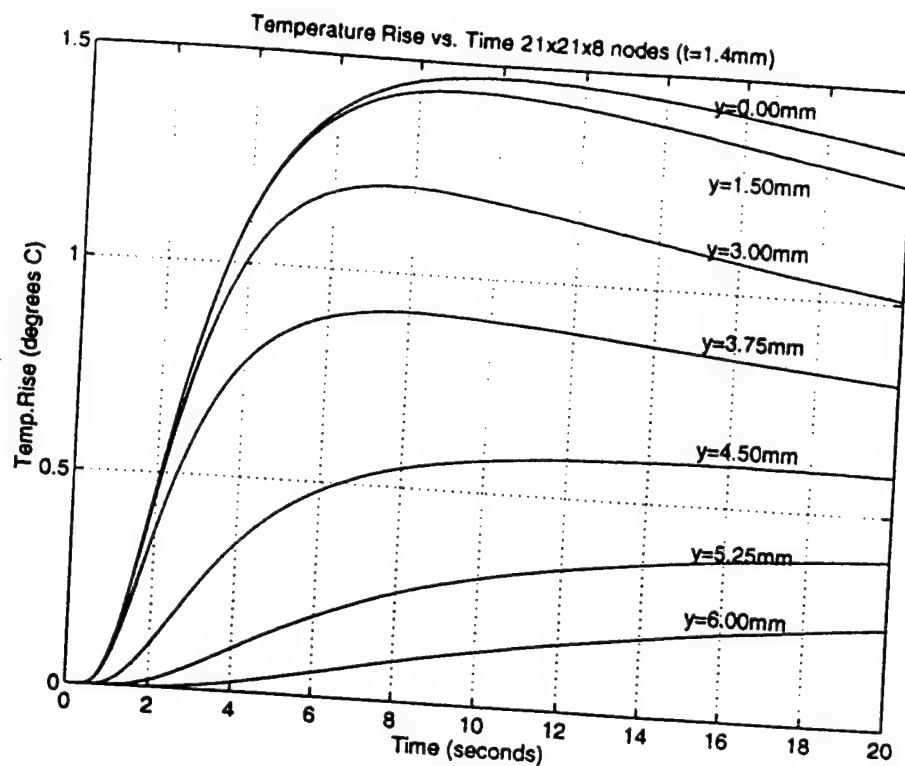


Figure 9. 1-D simulation results.

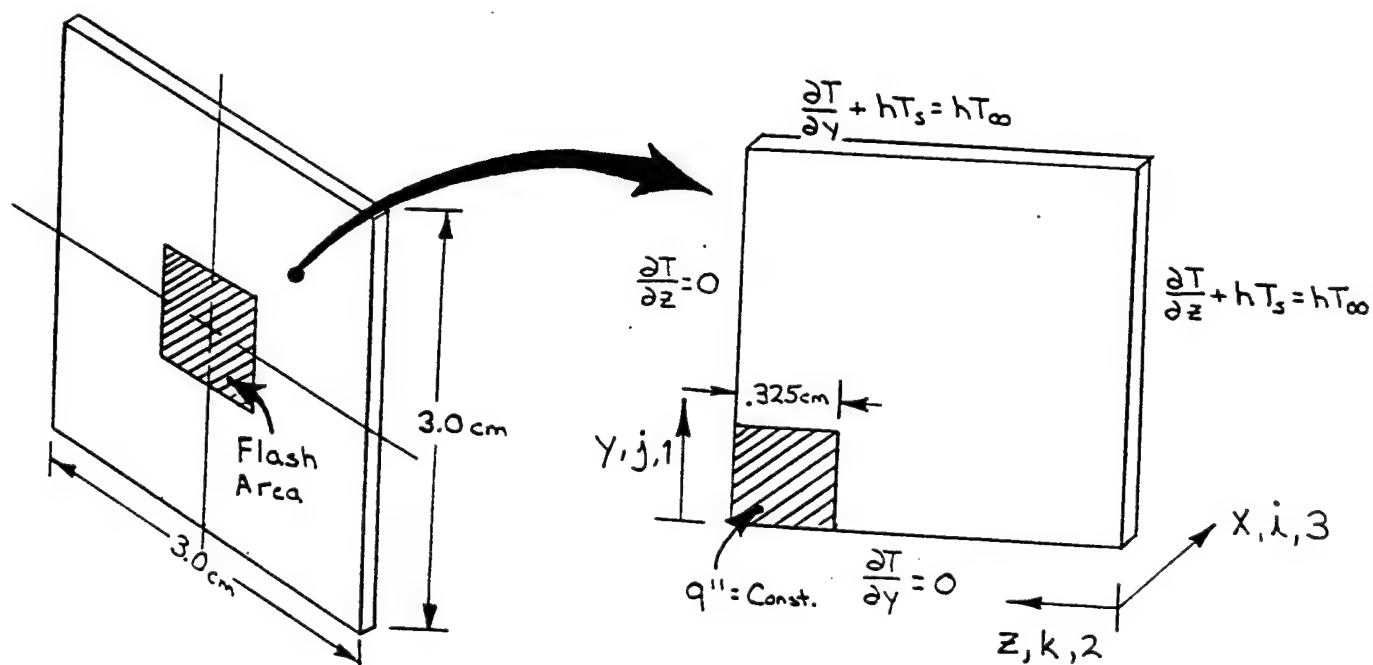


Figure 10. 3-D heat transfer simulation model.

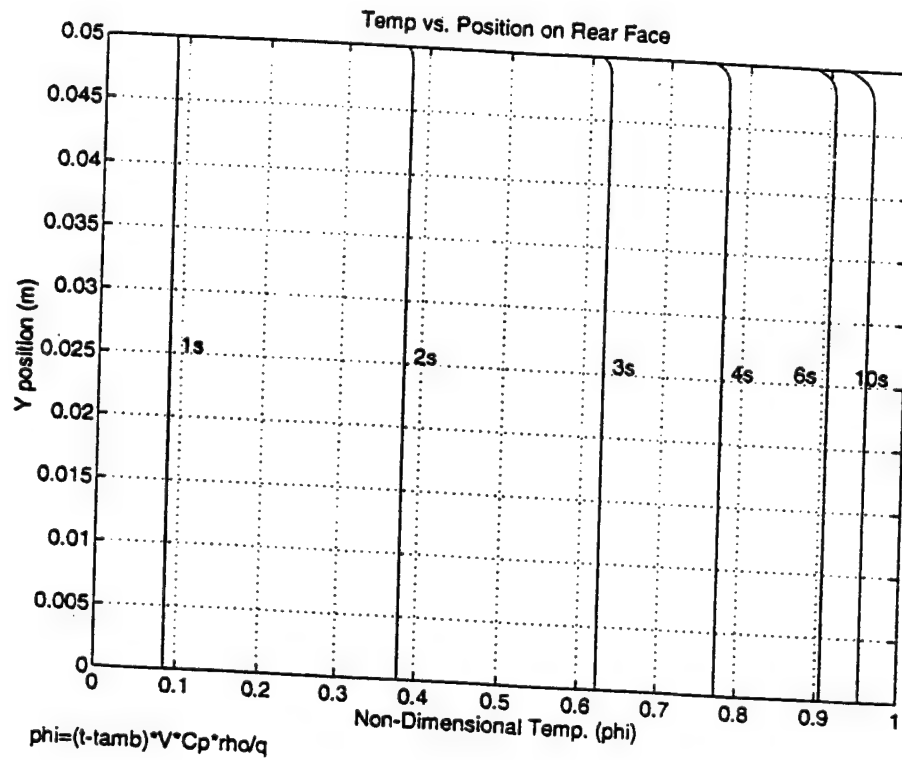
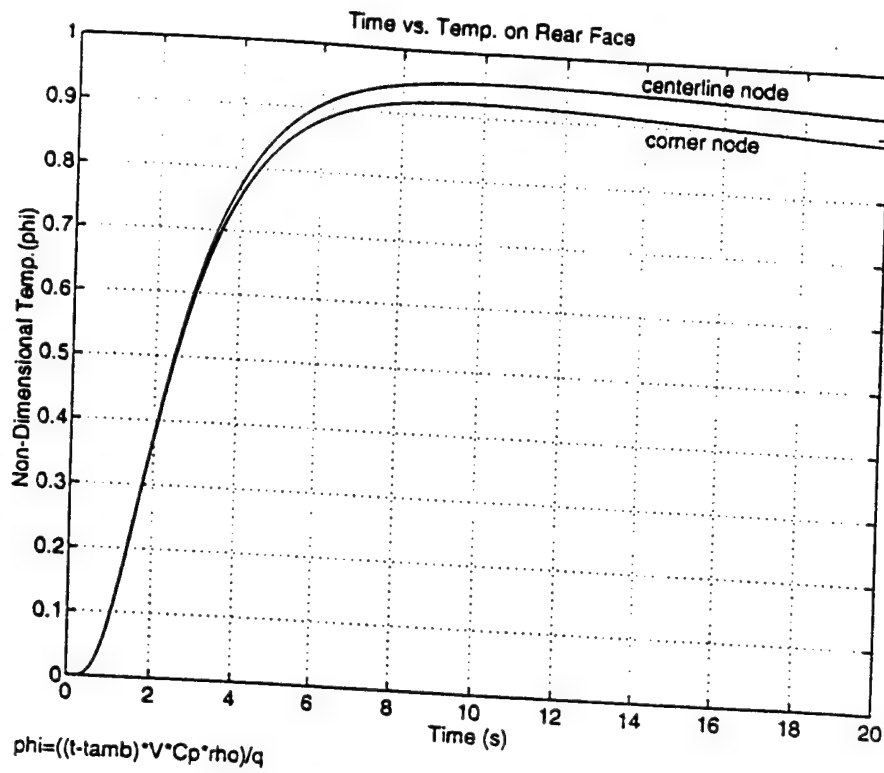


Figure 11. 3-D heat transfer simulation results.

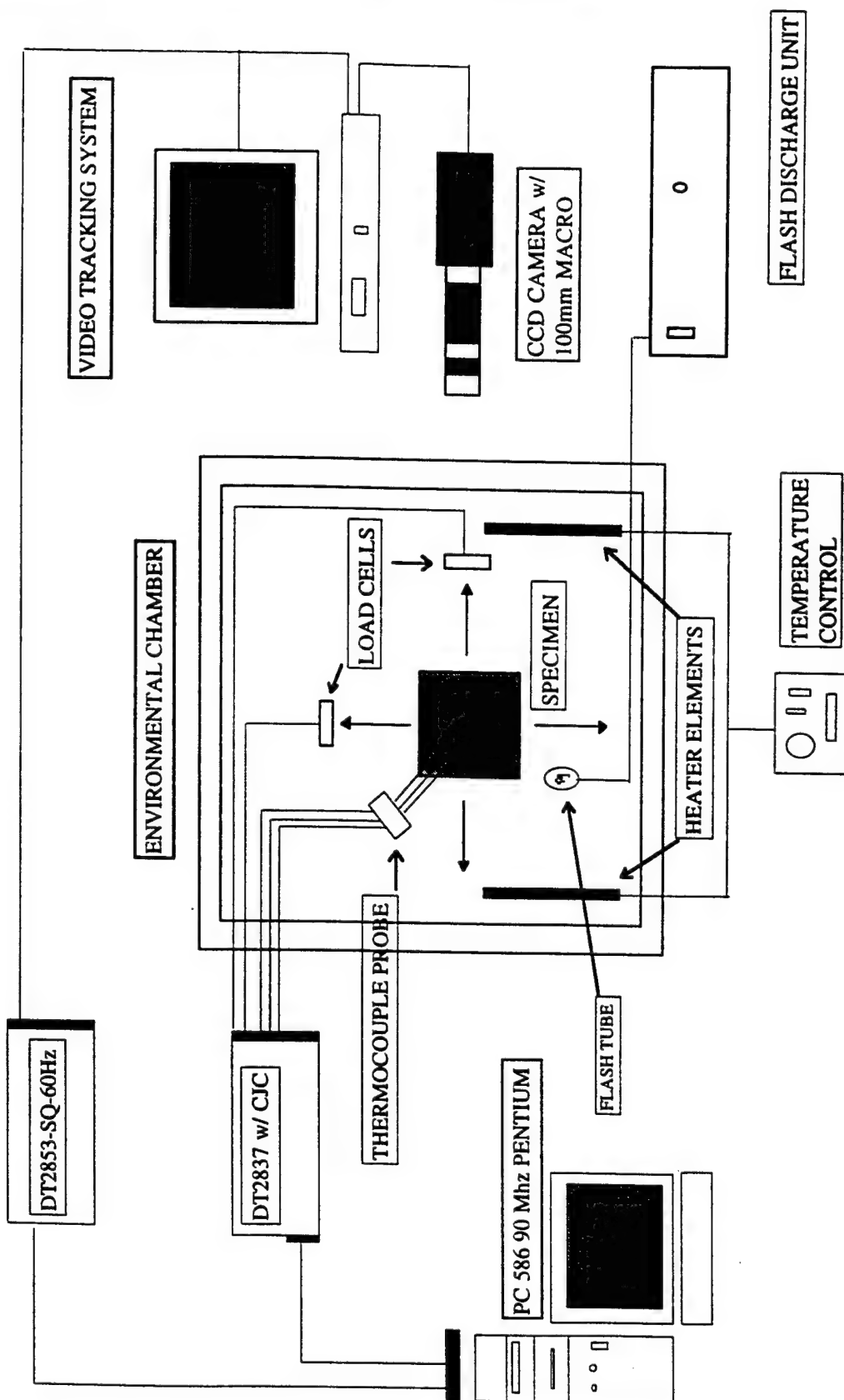


Figure 12. The overall experimental system.

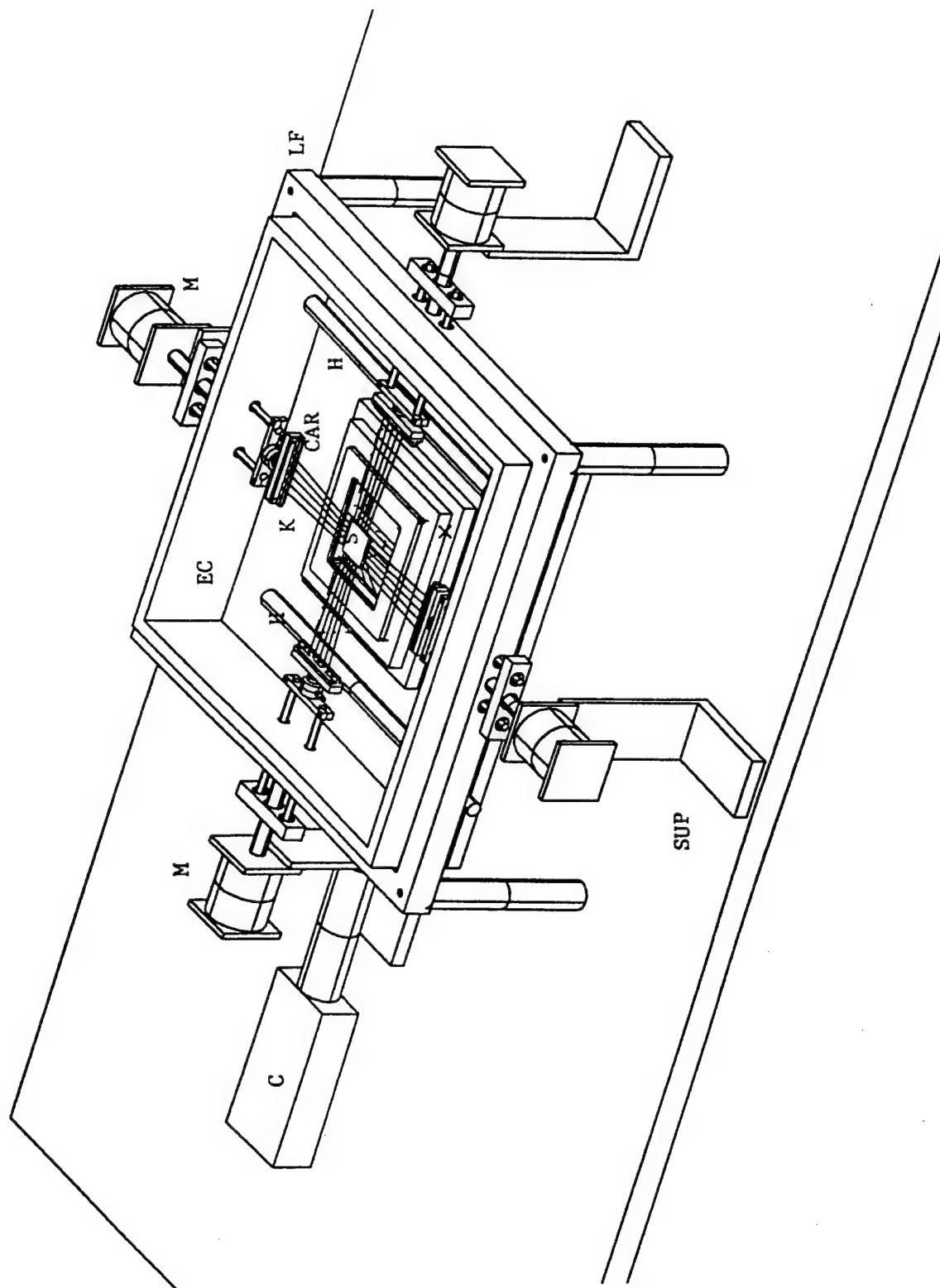


Figure 13a. Oblique view of the load frame (LF) and environmental chamber (EC).

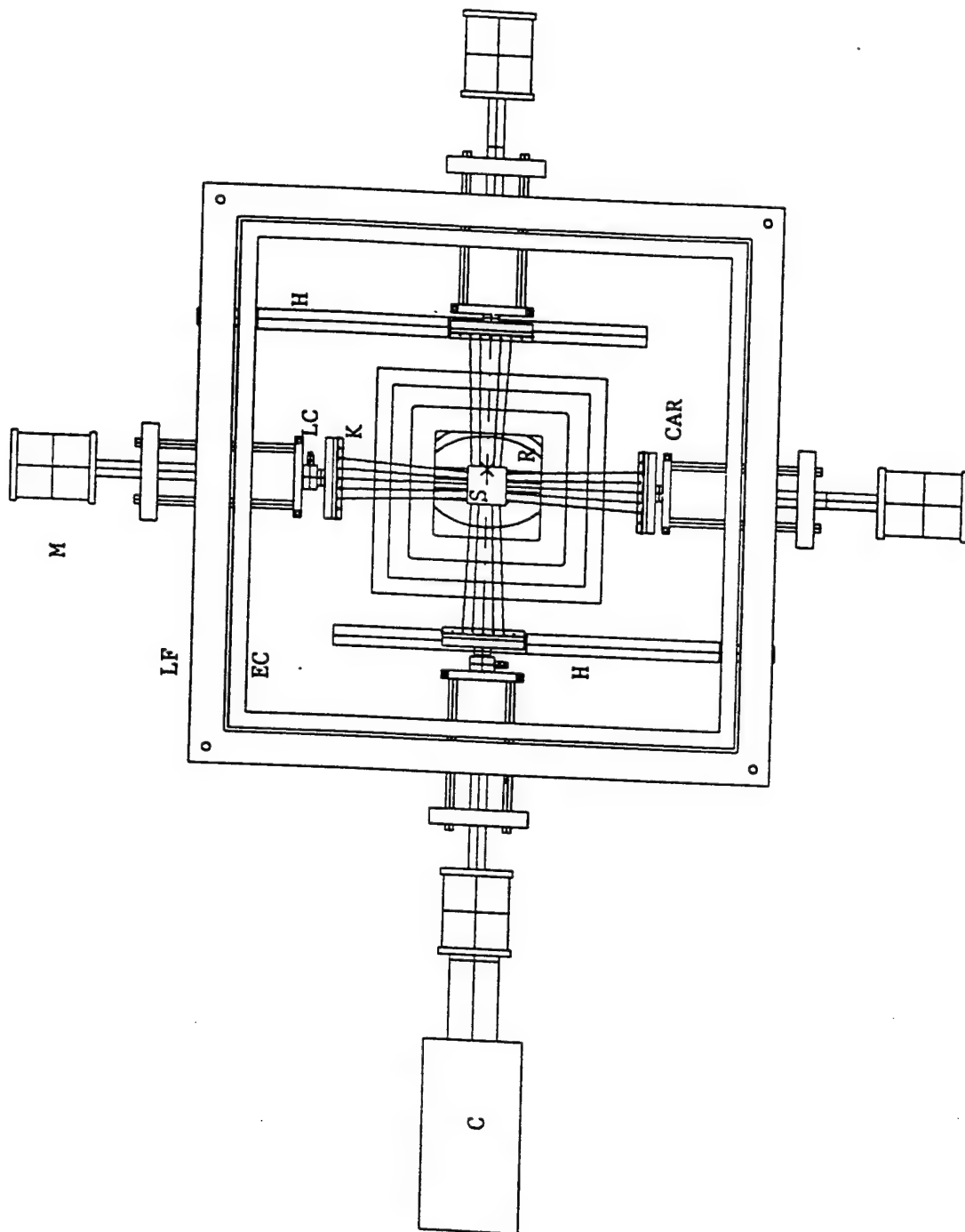


Figure 13b. Top view of the load frame (LF) and environmental chamber (EC).

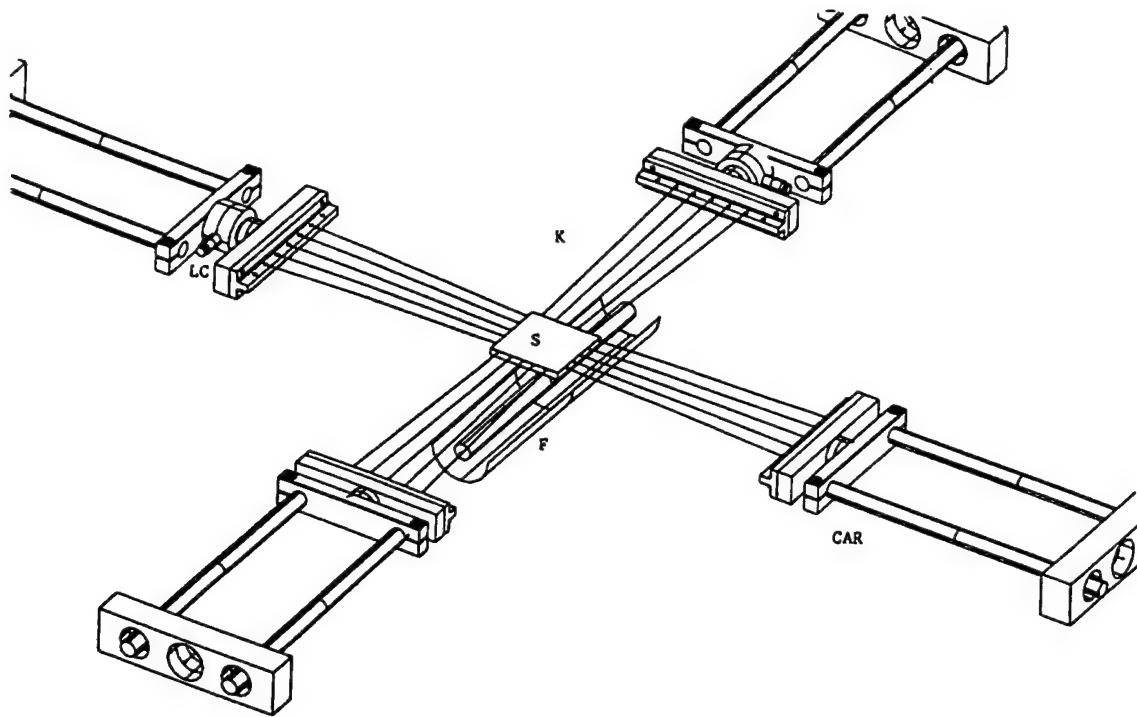


Figure 14. Close-up schema of the load carriage (CAR), load cell (LC), Kevlar attachment fibers (K), specimen (S), and flash tube/reflector assembly (F).

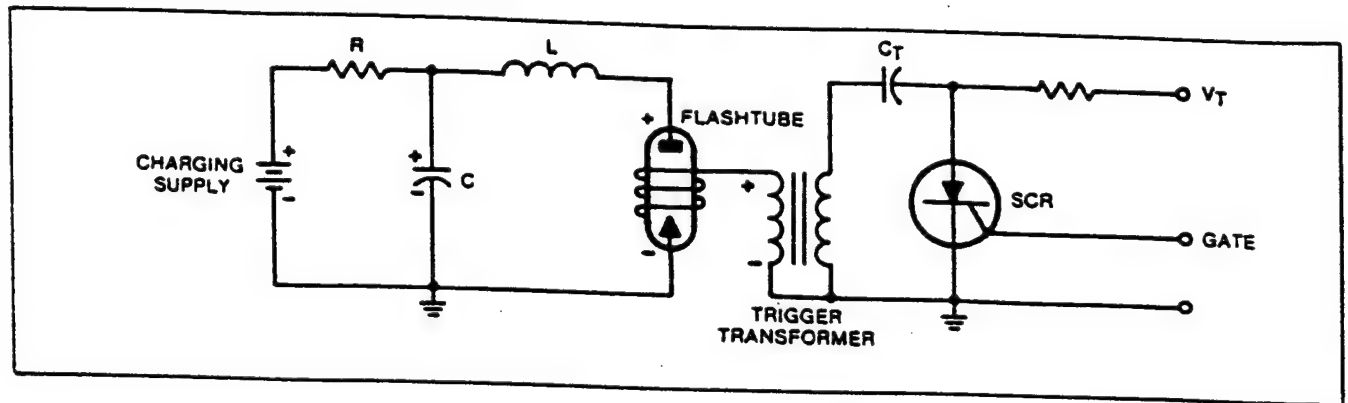


Figure 15. Circuit diagram for the flash tube.

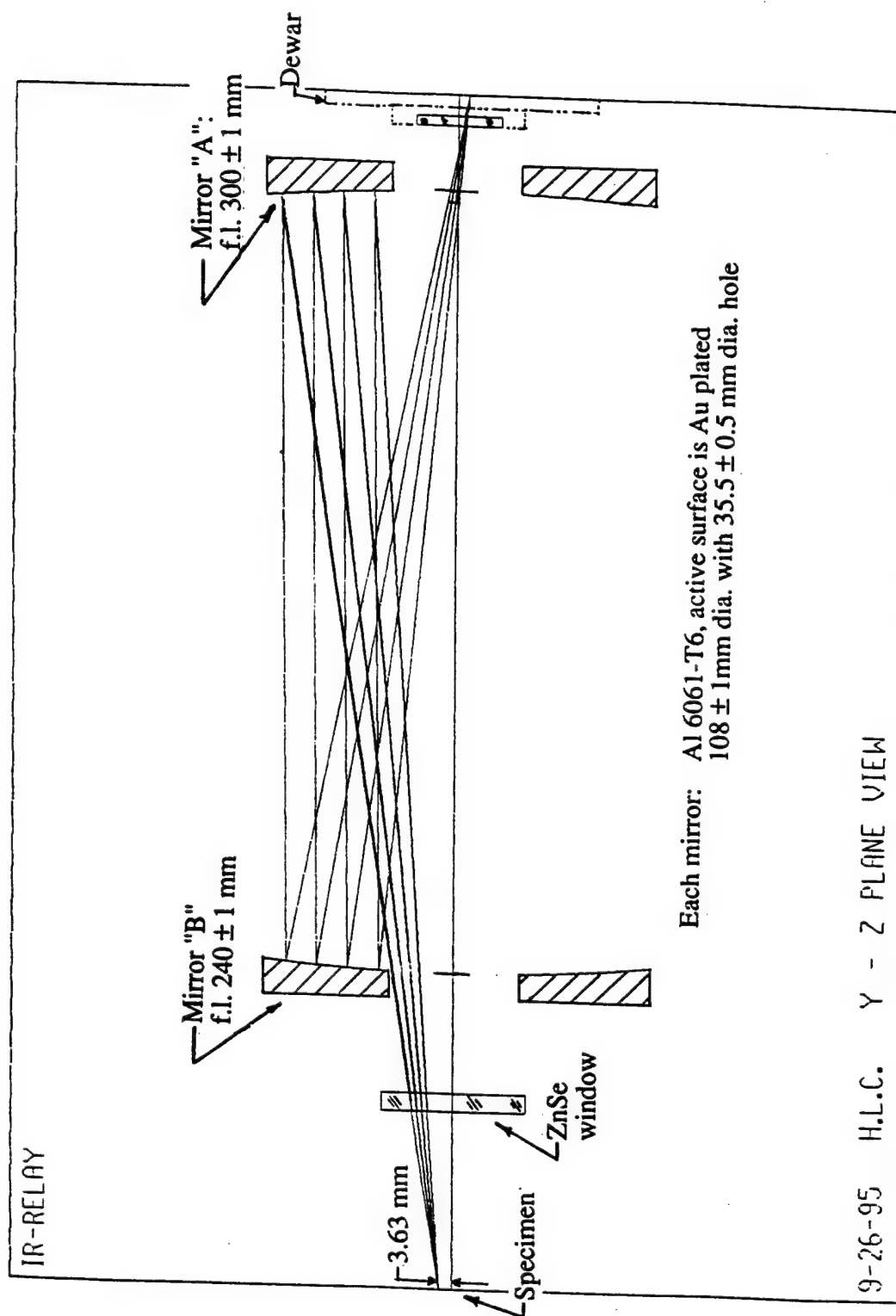


Figure 16. Ray tracing diagram of the infrared-relay optics designed to focus emissions from three points on the sample to three MCT detectors.

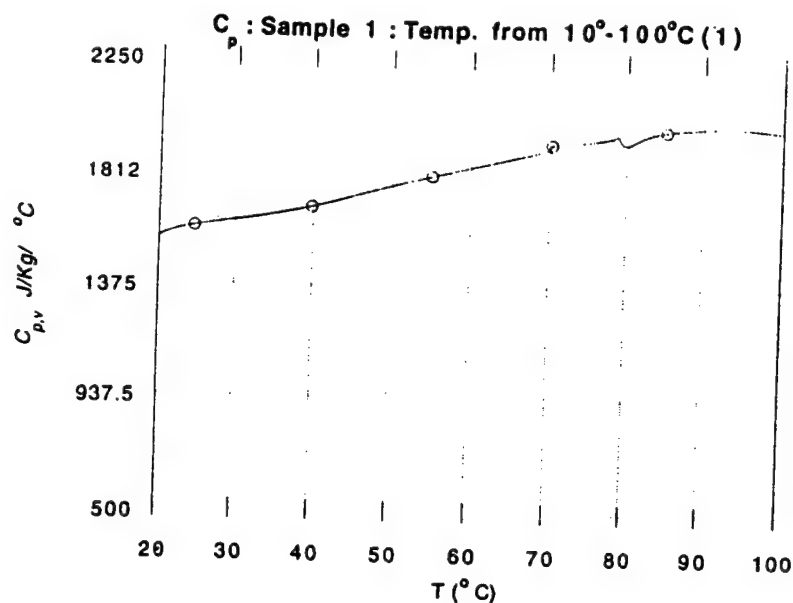


Figure 17. Dependence of the specific heat c_p of NGR on temperature measured using differential scanning calorimetry. Data in the unloaded configuration.

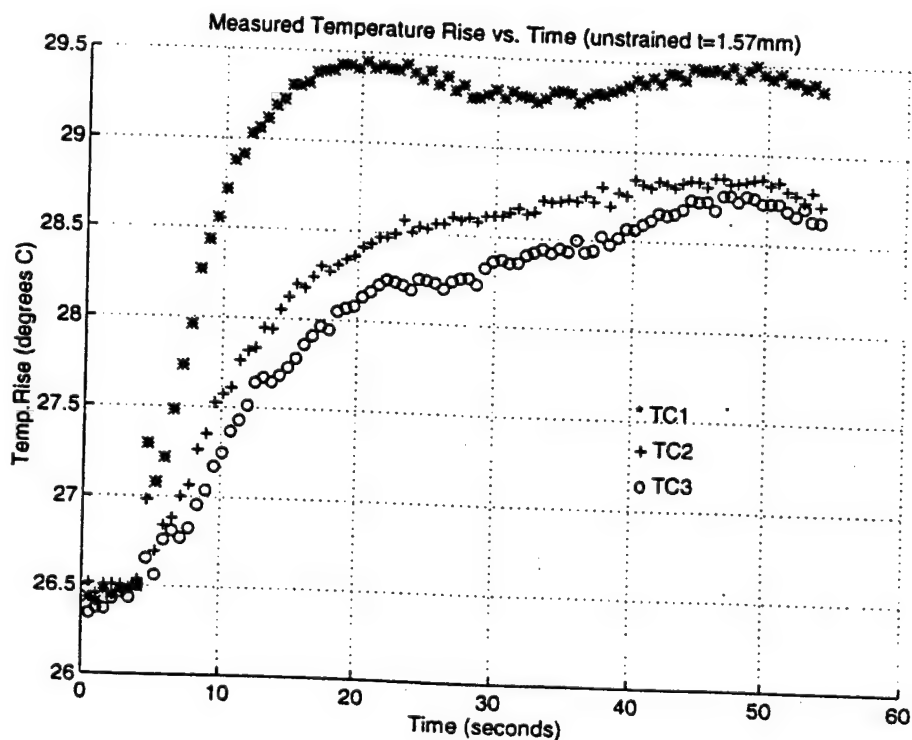


Figure 18. Temperature histories for a non-uniformly illuminated sample of NGR.

HIGH STRAIN-RATE BEHAVIOR AND DAMAGE MEASUREMENTS IN GLASS REINFORCED PLASTICS

A.S.Khan and P.K.Centala

Department of Mechanical Engineering
The University of Maryland
Baltimore., MD 21228-5398

ABSTRACT

Investigations comprising of experimental observations and analytical study have been systematically executed to evaluate a particular composite system which has the potential for structural armor applications. The material being a thick laminate, is a random mode stacking of bi-axial, plain weave S2-Glass/S2-Glass fiber yarns with polyester resin (Cycom 4102) as binder material, thirty two percent by weight. Attention is focused to understand the three dimensional macroscopic behavior of the material under quasi-static and dynamic compressive loading conditions. Quasi-static (low to medium strain rates) experimental investigations were carried out on an MTS test system while the dynamic response was observed using the Split Hopkinson Pressure Bar test equipment. The uniformity of the material's response is verified for different sized and shaped specimens. The material has been found to be transversely isotropic and its three dimensional stiffness matrix has been determined. The material's strength and strain rate effects in the region of 10^{-6} - 10^3 sec⁻¹ are also presented. The materials failure stress has been found to be higher under dynamic loads. The failure mechanism for the material in direction perpendicular to ply layup is fairly complex as compared to the other two orthotropic directions. Effort has been made to characterize the damage modes by investigating fractured surfaces.

INTRODUCTION

In continuing search for light weight materials of desirable strength and stiffness, considerable effort has been made in the past six decades in the technological development of fiber-reinforced materials⁽¹⁾. Their low specific gravities, the high strength-weight and modulus-weight ratios of these composite materials are markedly superior to those of metals⁽¹⁾. A potential for weight savings with fiber reinforced composites exists in many engineering fields, implementing them for actual use would necessitate rigorous design practices and viable process developments based on the understanding of their mechanical and physical characterization. Composite structural elements are now in a variety of components for automotive, aerospace, marine and architectural structures in addition to consumer products such as skis, golf clubs, tennis rackets, etc. One of the earliest and ever growing application area is in the military. It is well known that performance and maneuverability of vehicles (airborne or ground) depend substantially on weight. High specific strength and high specific stiffness characteristics of the composites encouraged the technical community to endeavor for its use in protective armor.

The first use of Glass fiber-reinforced plastic for armor applications⁽²⁾ occurred with the development of Doron^a which was employed by the US Marines during the Korean conflict. With the development of Kevlar^b, its applications ranged from Personal Armor systems such as fragmentation vest & helmets to spall liners within the M113 APC and Bradley Fighting Vehicles. S2-Glass reinforced plastic composite is now under consideration for combat vehicle hulls. For such a load bearing armor application it is but essential to evaluate the structural integrity and dynamic response of these composites. It is imperative that a complete understanding of the mechanical behavior of the composite system is made known and its behavior under different types of loading condition be predicted through simulations, before the material could be implemented for its desired application. The application is such that it is also necessary to understand the residual strength and performance of the composite system upon ballistic impacts.

Chou and Ko⁽³⁾ have illustrated that woven composites have proven to provide better stability in terms of strength and stiffness and extensibility than that of a unidirectional prepreg. This has interested researchers like Chen & Kuo⁽⁴⁾, Ishikawa⁽⁵⁻⁶⁾, Hashin, Rosen, Naik⁽⁷⁻⁹⁾ et al to conduct studies on 2-D woven SiC/SiC and C/SiC composites and have formulated their effective stiffness and strength. The above works are focussed on analytical and numerical results with plane stress and plane strain conditions. The strain in the thickness direction observed in such composites are significant and cannot be neglected from the stress-strain relation.

^aA laminate of fiber E-glass and polyester resin.

^bA high tenacity fiber developed by Dupont.

Naik and Ganesh⁽¹⁰⁾ carried out some shear strength studies on E-glass/epoxy resin plain weave fabric laminates. The experiments were confined to tensile loading at slow rates. Karayaka and Kurath⁽¹¹⁾ conducted failure studies on Graphite/Epoxy plain weave laminate under compression, tension and three point flexural loading. Kumar and Garg investigated failure modes in unidirectional E-glass-epoxy cross ply laminates under dynamic compression and characterized them fractographically. Again the samples investigated in the above cases were from laminates whose thickness were less than 3mm. Dandekar, Green and Beaulieu⁽²⁾ had carried out studies on thick S2-GRP to determine the elastic constants through ultrasonic techniques and had characterized the material to be transversely isotropic. They also performed quasi-static tests in compression & tension along with some high strain rate experiments in the thickness direction.

As mentioned previously, identifying the onset of damage and its evolution while the composite is under load or upon impact is being further evaluated. Understanding the damage mechanics is very useful as it can aid to predict the residual strength of the composite and its response to subsequent loads/impacts. Damage development studies in unidirectional graphite/epoxy cross-ply laminates were carried out by Daniel and Lee⁽¹³⁾. Damage was characterized by the classical decreasing stiffness notation and its correlation to fiber failure and matrix cracking. Shan, Pulvinage⁽¹⁴⁾ et al reported analysis and modelling of damage behavior of two-dimensional woven SiC/SiC composites. Their work was supported by numerical results. Degradation of the elastic properties of matrix, fiber and interfacial bonding was considered as a measurement for the evolution of damage. This classical approach of relative variation of elastic properties as an indicator of damage cannot predict the origin of damage and its location. Acoustic emission detection technique, upon careful monitoring can provide us with information pertaining to the origin, evolution and location of damage. Sachse and Kim⁽¹⁵⁾, and Liao and Targ⁽¹⁶⁾, Gardiner and Pearson⁽¹⁷⁾ have all contributed to use of acoustic emission in understanding material properties variation and monitoring of damage occurring under static loading. Their work was focussed on graphite/epoxy unidirectional laminates and involved the traditional acoustic emission parameters such as amplitude, count, energy, time, etc., to quantify the failure mechanisms. Conventional AE methods employed resonant sensors and narrow band pass filters. This type of measurement discards much of the information available. With recent advances in technology, it is now possible to perform wave based AE measurements, along with high fidelity and broad band sensors. This allows to analyze the damage occurrences and its evolutions based on the physical dynamics of the micro-structure of the composite material. Gorman⁽¹⁸⁾ in his paper presents a comparative illustration between the old AE method and the new wave based AE method. The damage evaluation experiments using the wave based acoustic emission equipment is presently being carried out in the laboratory.

EXPERIMENTAL PROCEDURE

(i) Material

The material constituents in the composite are S2-Glass in the fiber form and Polyester resin(CYCOM 4102) as the binder or matrix. The construction of the composite is as follows:

Yarn : The yarn(see Fig.1) is a collection of parallel continuous ends of fibers of average diameter of 10 microns. The fibers are so gathered to give the yarn an approximate elliptical cross-section with the ratio of major to minor axis being around 10 . Yarn typically consists of approximately 10^{10} fibers bundled together. A binder material is distributed in the inter fiber space to the desired volume fraction.

Lamina : The lamina(see Fig.2) is a two dimensional plain weave balanced construction of the fiber yarns in the two mutually perpendicular direction. 'Wrap yarn' is termed for the yarn in one weave direction and 'fill yarn' for the yarn in the other perpendicular weave direction. The woven construction is then impregnated with the polyester resin in the inter-yarn space so as to obtain a lamina of uniform thickness. The lamina measured 0.68mm in thickness.

Laminate : The laminate(see Fig.3) is a random phase mode multi-layer(42 ply) stacking of such laminas such that the wrap and fill yarns align in the same directions. The stacked lamina is then cured under desired pressure and temperature cycle in an autoclave. The material was in plate form(51cmx51cm) having 42 plies and measured 26.4mm in thickness. The materials density was found to be $1.92 \pm 0.03 \text{ gm/cm}^3$. The resin content was 32 ± 2 percent by weight. The properties of CYCOM 4102 along with the fiber volume fraction in the material construction are provided in Table 1.



Fig.1:Yarn

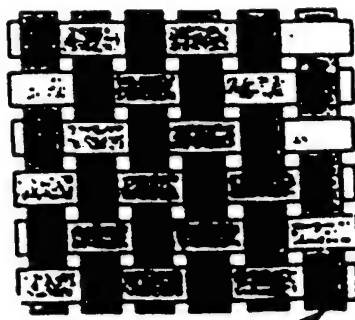


Fig.2: Lamina

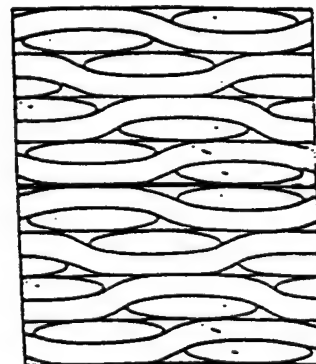


Fig.3 :Laminate

The fiber orientation and ply lay-up suggests that the material mechanical response would be orthotropic. Three orthotropic directions(see Fig.4) were identified namely, [100] Direction - along

the axis of the wrap yarn, [010] Direction - along the axis of the fill yarn and [001] Direction-perpendicular to the lamina plane

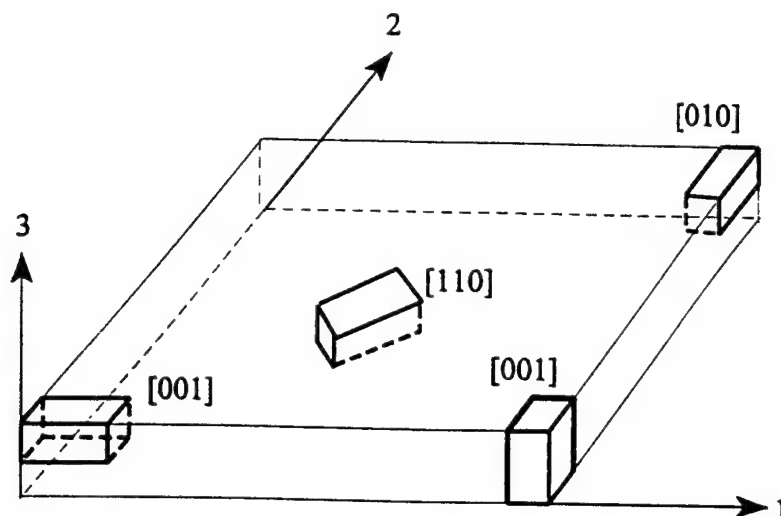


Fig.4 Orientation of Specimens

The composite was observed not to absorb moisture. In machining the test specimens Kennametal KC730 Titanium Nitride and Diamond Carbide cutting tools were employed.

Table 1

	Density gm/cm ³	Modulus GPa	Strength MPa	Weight Percent	Volume Percent
S2-Glass Fiber (10-12 microns dia.)	2.49	85.5	4585	68	52.37
Polyester Resin (CYCOM 4102)	1.3	3.6	78.5	32	47.63

(ii)QUASI-STATIC COMPRESSION TESTS

The material's mechanical response in compression was investigated. The quasi-static(low to medium strain rates) compression experiments were carried out in the MTS material test equipment. The MTS809 is a servo-hydraulic controlled axial/torsion test equipment with a 250kN/2200Nm static load/torque capability. The controller to the MTS is interfaced with a computer and Teststar SX-790.10 is the software module used to program the compression experiments. The hydraulic actuators of the MTS can be programmed to move linearly in a

continuous range from 10^{-6} to 3 in/sec. Force measurements were made by means of load cell on the MTS and the strains were monitored using strain gages and the MTS LVDT. The strain gage data was used in the strain region of interest. In higher strain regions the LVDT data along with the correction factor was used. The force, displacement and the strain readings were acquired continuously through the data acquisition built in the controller computer. It had the capability of collecting data every 0.001 second. The load cell and the LVDT were calibrated and the error in the readouts were less than 2 percent in the range of 200kN force and 25 mm displacement.

Preliminary experiments were conducted to investigate the shape and size effects on specimen as the material was not microscopically homogeneous. Two types of geometries were selected i.e. circular cross-section and square cross-section. Two different sizes were chosen for each geometry. Fig. 4 gives the details of the specimens tested for this purpose. In all of the samples, three types of specimen orientation were machined such that the loading axis corresponded to the three orthotropic directions. Table 2 summarizes the results and Figs. 5 & 6 illustrate the material's directional elastic responses. All specimens were loaded in compression under a constant strain rate of 10^{-4} sec^{-1} . Teflon sheet (0.127mm thickness) was used at the specimen ends for lubrication.

In compression tests to evaluate the elastic constants of the material, specimens with square cross-section measuring 12.7x12.7 mm and 25.4 mm long, were chosen. In addition to the three specimen orientation chosen earlier, the [110] orientation specimen were also used. Two element rosettes (KYOWA Electronic Instruments Co., Ltd., Japan) of 5 mm gage length were mounted on 3 adjacent vertical surfaces. The strain readings from the four gages on adjacent faces would describe the axial strain in the loading (one orthotropic) direction and its corresponding transverse strains in the other two orthotropic direction. The measured elastic constants from these test are given in Table 3.

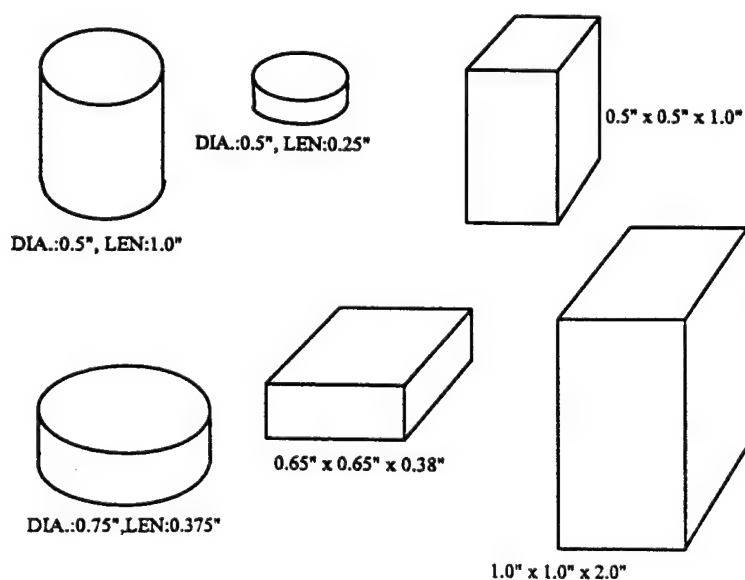


Fig 4. Specimen samples

Next the material's responses for different strain rates i.e. 10^{-5} sec^{-1} , 10^{-2} sec^{-1} and 10^0 sec^{-1} , were investigated in all three orthotropic directions. Fig.7- 10 illustrate the results of these tests.

(iii) DYNAMIC RESPONSE EXPERIMENTS

The dynamic response of the material was investigated under high strain rate compressive loading by means of split Hopkinson Pressure Bar test equipment. The impacting bar was 56 cms long which resulted in a loading pulse of about 220 micro-seconds. The impacting bar is propelled out of a gas gun, using compressed nitrogen gas. The magnitude of the loading pulse was a function of the firing pressure. Strain rates upto 10^3 was attained in these experiments. The incident and transmitted bars diameter was 0.99 inch. By means of strain gages on the incident and transmitted bars, the strain-time histories of the three pulses, incident, reflected and transmitted were recorded on a Nicolet 440 digital oscilloscope with 12 bit digitization and sampling rates as low as 0.1 micro-second. The nominal stress and strain in the specimen upto any time duration t , was determined by using standard relations given below, for this technique.

$$\epsilon_s = - \frac{c_o}{L_o} \int_0^t (\epsilon_I - \epsilon_R - \epsilon_T) dt \approx - 2 \frac{c_o}{L_o} \int_0^t \epsilon_R dt \quad (1)$$

$$\sigma_s = \frac{1}{2} E_B \frac{A_B}{A_s} (\epsilon_I + \epsilon_R + \epsilon_T) \approx E_B \frac{A_B}{A_s} (\epsilon_T) \quad (2)$$

However, information within the strain regions of 2% cannot be considered accurate in this technique. The specimen were cylindrical disks and two different sizes were tested in the [001] directions. One specimen size was measuring 19 mm in diameter and 9.6mm thick and the other was measuring 12.7mm in diameter and 6.35mm thick. Specimen samples in the [100] and [010] orthotropic directions were of the same size being 19mm in diameter and 9.6mm thick. Table 4 gives the details of the specimens and the average strain rates applied in the experiments.

RESULTS AND DISCUSSION

Quasi-Static Response

The material's response did not significantly change due to size or shape of the specimens tested, although there was about 12 percent variation between maximum and minimum moduli values as seen in Table 2. This variation cannot be identified as a size effect because a similar observation is made in Table 3 for specimens of the same geometry and size. This variation suggests that the nature of the micro-inhomogeneities within the material which is inherent due to the manner

in which the material was fabricated. The materials elastic response in the [100] and [010] direction was observed to be very similar and linear. The average modulus in the [100] direction was determined as $29.67 \pm 3.65 \text{ GPa}$ and that in the [010] direction was determined as $30.06 \pm 1.74 \text{ GPa}$. Dandekar⁽²⁾, et al. in their studies had reported a variation in the modulus from 26.3 to 47.5 GPa in [100] and from 24.5 to 43.0 GPa in

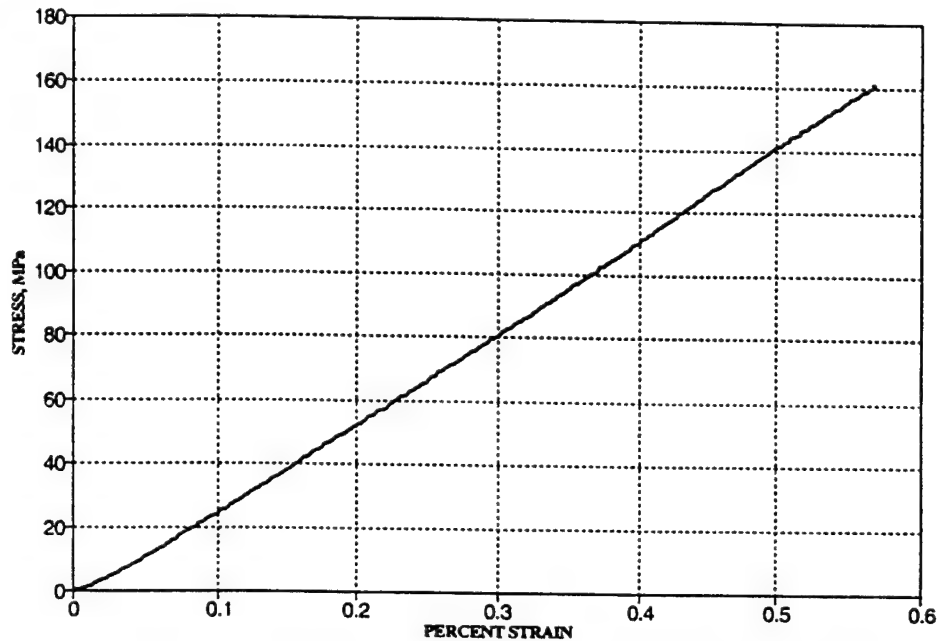


Fig.5 : Response of [100] and [010] orientation specimens

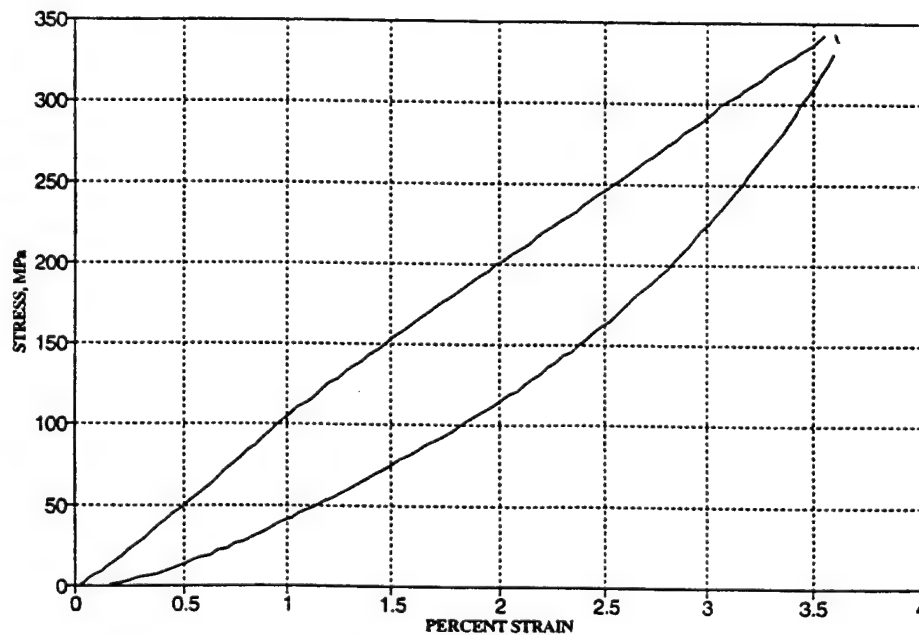


Fig.6: Response of [001] orientation specimens

Table 2

SPECIMEN	DIMENSIONS	ELASTIC RESPONSE	MODULI(GPa)	
MTS_X1	0.5"x 0.5"x 1.0"	LINEAR	29.62	
MTS_X2	0.5"x 0.5"x 1.0"	LINEAR	29.26	
MTS_X3	1.0"x 1.0"x 2.0"	LINEAR	29.48	
MTS_X4	1.0"x 1.0"x 2.0"	LINEAR	31.11	
MTS_X5	DIA. 0.5" x 1.0"	LINEAR	33.33	
MTS_X6	DIA. 0.5" x 1.0"	LINEAR	31.42	
MTS_X7	0.65"x 0.65"x 0.4"	LINEAR	26.67	
MTS_X8	0.65"x 0.65"x 0.4"	LINEAR	28.77	
MTS_X9	DIA. 0.75"x 0.4"	LINEAR	28.0	
MTS_X10	DIA. 0.75"x 0.4"	LINEAR	29.09	
MTS_Z1	0.5"x 0.5"x 1.05"	APP. LINEAR	13.05	
MTS_Z2	0.5"x 0.5"x 1.05"	APP. LINEAR	14.5	
MTS_Z3	DIA. 0.75 x 2.0"	APP. LINEAR	11.25	
MTS_Z4	DIA. 0.75 x 2.0"	APP. LINEAR	10.65	
MTS_Z5	DIA. 0.5" x 1.05"	APP. LINEAR	11.76	
MTS_Z6	DIA. 0.5" x 1.05"	APP. LINEAR	12.73	
MTS_Z7	0.65"x 0.65"x 0.4"	APP. LINEAR	16.11	
MTS_Z8	0.65"x 0.65"x 0.4"	APP. LINEAR	11.38	
MTS_Y1	0.5"x 0.5"x 1.0"	LINEAR	28.32	
MTS_Y2	0.5"x 0.5"x 1.0"	LINEAR	29.56	
MTS_Y3	1.0"x 1.0"x 2.0"	LINEAR	30.12	
MTS_Y4	1.0"x 1.0"x 2.0"	LINEAR	30.81	
MTS_Y5	DIA. 0.5" x 1.0"	LINEAR	31.02	
MTS_Y6	DIA. 0.5" x 1.0"	LINEAR	30.14	
MTS_Y7	0.65"x 0.65"x 0.4"	LINEAR	29.45	
MTS_Y8	0.65"x 0.65"x 0.4"	LINEAR	30.13	
MTS_Y9	DIA. 0.75"x 0.4"	LINEAR	29.67	
MTS_Y10	DIA. 0.75"x 0.4"	LINEAR	31.38	

Table 3

SPECIMEN	MODULUS Gpa	POISSONS RATIO		Failure Strain, %	Failure Stress, MPa
MTS_X1	28.99	$V_{12}=0.12$	$V_{13}=0.34$	1.02	208.5
MTS_X2	30.85	$V_{12}=0.11$	$V_{13}=0.37$	1.12	232.3
MTS_X11	31.27	$V_{12}=0.14$	$V_{13}=0.35$	0.87	187.4
MTS_X12	32.78	$V_{12}=0.12$	$V_{13}=0.34$	1.17	245.3
MTS_X13	30.67	$V_{12}=0.12$	$V_{13}=0.35$	1.04	228.3
MTS_Y1	28.32	$V_{21}=0.12$	$V_{23}=0.34$	0.98	215.6
MTS_Y2	29.56	$V_{21}=0.10$	$V_{23}=0.32$	1.06	236.8
MTS_Y11	30.12	$V_{21}=0.13$	$V_{23}=0.38$	1.20	252.3
MTS_Y12	32.02	$V_{21}=0.12$	$V_{23}=0.35$	1.16	248.3
MTS_Y13	31.23	$V_{21}=0.14$	$V_{23}=0.34$	1.11	243.5
MTS_Z1	14.36	$V_{31}=0.18$	$V_{32}=0.16$	6.83	620.6
MTS_Z2	10.67	$V_{31}=0.17$	$V_{32}=0.19$	7.43	680.3
MTS_Z9	12.62	$V_{31}=0.19$	$V_{32}=0.18$	7.56	690.6
MTS_Z10	11.95	$V_{31}=0.19$	$V_{32}=0.18$	7.31	611.6
MTS_Z11	11.22	$V_{31}=0.19$	$V_{32}=0.18$	8.32	703.1
MTS_XY_1	13.37	-----	-----	-----	-----
MTS_XY_2	14.05	-----	-----	-----	-----
MTS_XY_3	13.83	-----	-----	-----	-----
MTS_XY_4	12.78	-----	-----	-----	-----
MTS_XY_5	13.23	-----	-----	-----	-----

[010]directions. It was noticed that the response was linear elastic until failure in both of these directions. Failure is characterized by multiple delaminations and loss of structural integrity. The average failure stress for [100] specimens was found to be 220.36 ± 28.88 MPa and that for the [010] specimens was 239.3 ± 18.35 MPa as compared¹ to 212.9 ± 23.2 and 210.3 ± 46.2 MPa, respectively. The average failure strains recorded were 1.04 and 1.10 percent in the [100] and [010] orientation as again compared^c to $0.76 \pm 0.18\%$ and $0.89 \pm 0.04\%$, respectively. The Poissons ratio was higher in the [001] direction with a average value of 0.35.

^cDandekar, et.al., Army Research Laboratory report⁽²⁾

The material's response in the [001] specimens was very different from that of the [100] and the [010] specimens. The modulus was much lower and the average value was 12.67GPa. Slight non-linearity is observed during loading and the unloading occurs on a different stress-strain loci and is more non-linear. Only the loading stress-strain region is used to compute the modulus in this direction. This difference in the loading and unloading stress-strain region is due to the polymer matrix dominance in this direction of deformation and the polymer matrix is visco-elastic in nature. This also pertains to the lower modulus in this direction. The failure stress and strains have been found to be much higher than that in the [100] and [010] directions. A lower dispersion in the failure stresses and strains is observed and the average values for the failure stress being 660.8 ± 41.24 Mpa and that for failure strain being 7.49 ± 0.83 percent.

The failure mode in this direction is much more complicated. Most of the specimens failed in the mid region and across one or two shear planes. Fiber yarn fracture, matrix cracking and delamination were all coupled to result in a catastrophic failure. Blackened regions were observed in the shear area indicating possible temperature rise (Fig.12). Figures 10-13 show the photo micrographs of failed surfaces of specimens.

The material's strain rate dependence in the [001] direction is much more than that observed in the [100] and [010] directions for the strain rates region 10^{-6} to 10^0 . This is observed from fig7-fig.9.

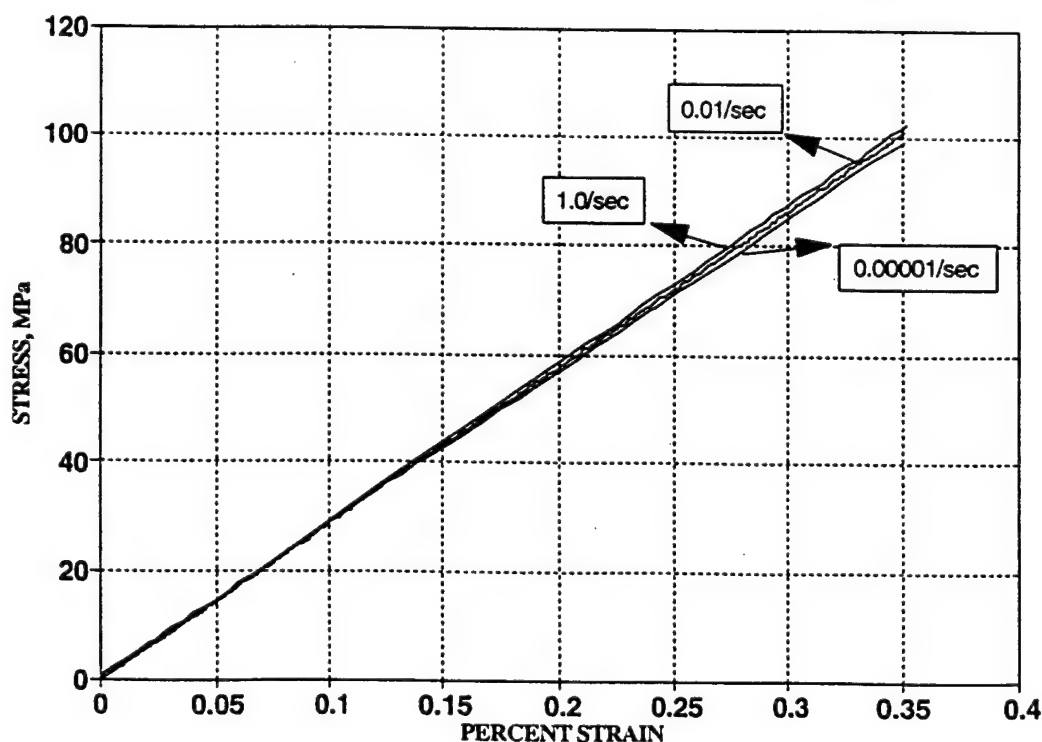


Fig.7: Effect of strain rate in [100] orientation specimens

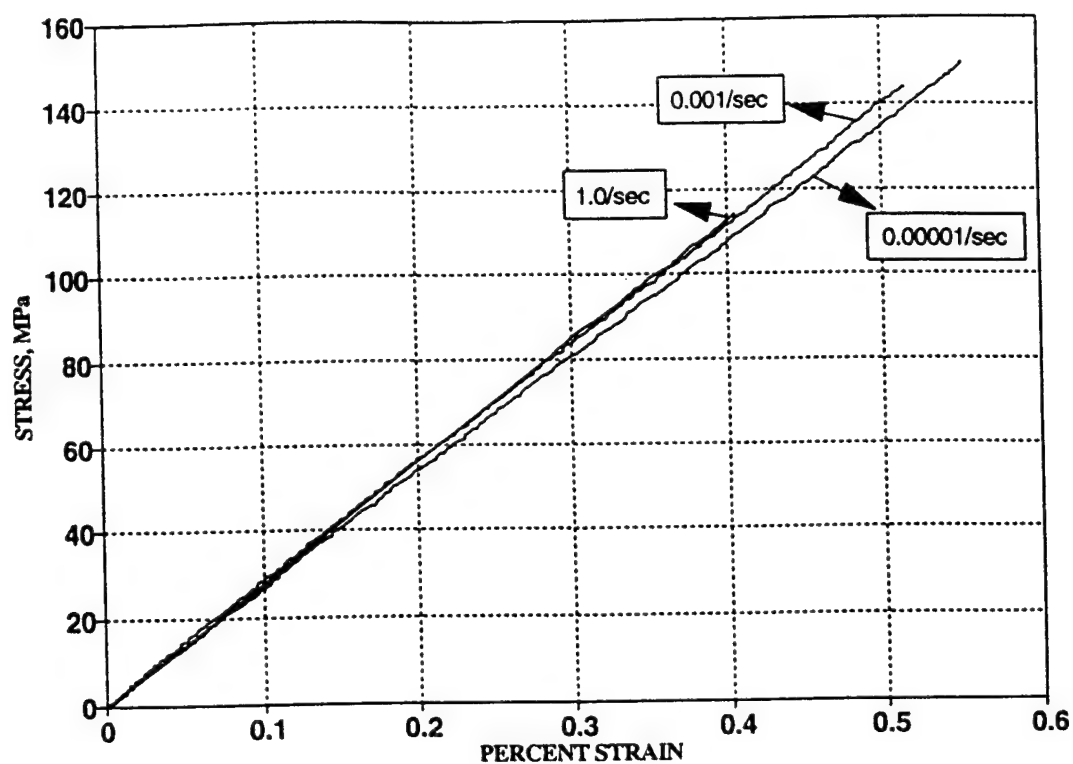


Fig.8: Effect of strain rate in [010] orientation specimens

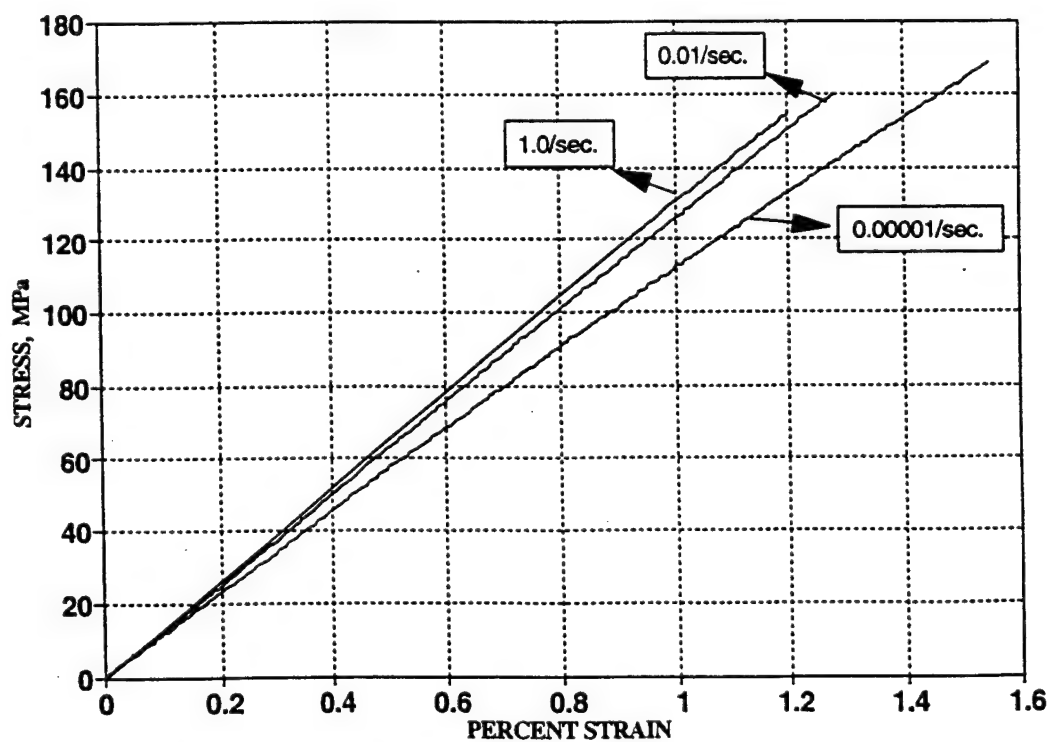


Fig.9: Effect of strain rate in [001] orientation specimens



Fig.10: Photomicrograph(20X) of a failed [001] specimen under quasi-static compression. Failure has occurred across two adjacent shear planes



Fig.11: Photomicrograph(12X) of failed [001] specimen's surface, viewing from top illustrating fiber yarns rupture along the shear plane.



Fig.12: Photomicrograph(15X) of a failed [001] specimen under quasi-static compression, viewing from the top. Dark regions suggest temperature rise during deformation.

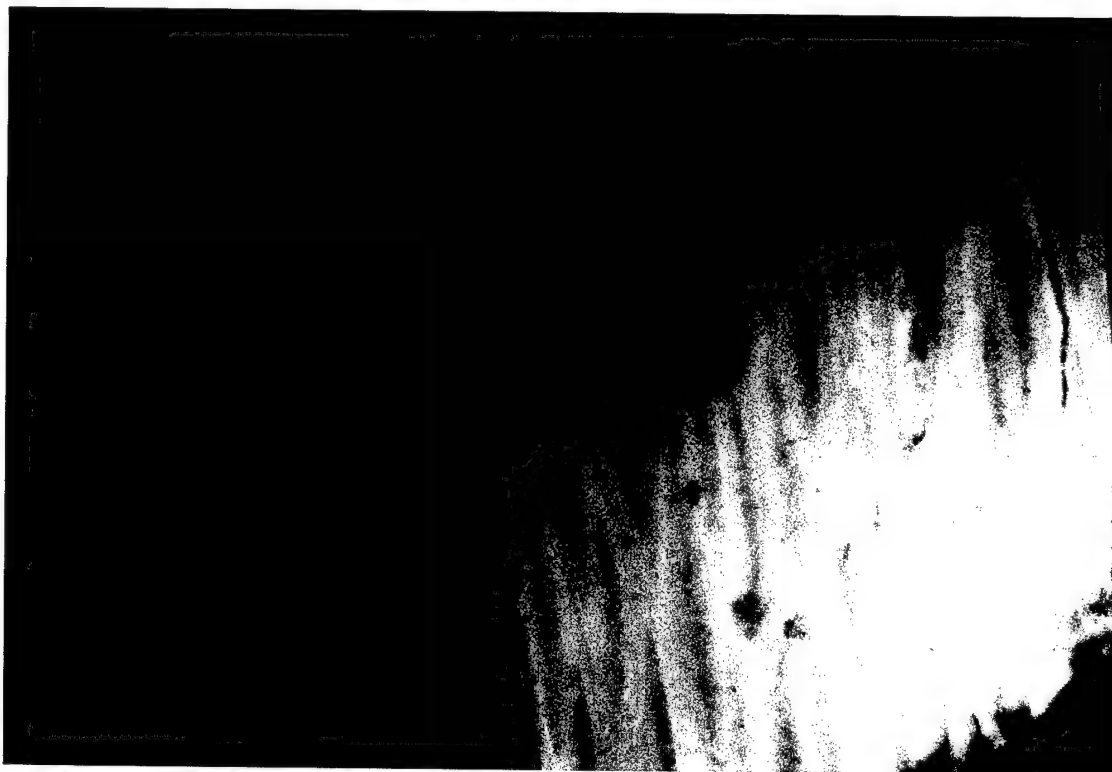


Fig.13: Photomicrograph(20X) of failed [100] specimen's surface characterizing delamination as the failure mode.

Dynamic Response

Table 4 gives a listing of specimens details with average strain rates applied in the Split hopkinson pressure bar tests and the failure stress, if failure occurred.

Table 4

Specimen No.	Orientation	Specimen Dimensions	Strain Rates	Failure stress MPa
SHPB-22	[001]	Dia. = 0.50", Th. = 0.25"	313	--
SHPB-17	[001]	Dia. = 0.50", Th. = 0.25"	434	--
SHPB-18	[001]	Dia. = 0.50", Th. = 0.25"	483	--
SHPB-27	[001]	Dia. = 0.50", Th. = 0.25"	506	--
SHPB-16	[001]	Dia. = 0.50", Th. = 0.25"	690	910
SHPB-15	[001]	Dia. = 0.50", Th. = 0.25"	1182	924
SHPB-28	[001]	Dia. = 0.50", Th. = 0.25"	1610	970
SHPB-5	[001]	Dia. = 0.75", Th. = 0.375"	418	--
SHPB-25	[001]	Dia. = 0.750", Th. = 0.375"	516	--
SHPB-9	[001]	Dia. = 0.750", Th. = 0.375"	610	--
SHPB-26	[001]	Dia. = 0.750", Th. = 0.375"	639	--
SHPB-29	[001]	Dia. = 0.750", Th. = 0.375"	772	--
SHPB-13	[001]	Dia. = 0.750", Th. = 0.375"	924	
SHPB-8	[100]	Dia. = 0.750", Th. = 0.375"	148	185
SHPB-20	[100]	Dia. = 0.750", Th. = 0.375"	320	245
SHPB-21	[100]	Dia. = 0.750", Th. = 0.375"	290	203
SHPB-24	[010]	Dia. = 0.750", Th. = 0.375"	543	270
SHPB-23	[010]	Dia. = 0.750", Th. = 0.375"	348	190
SHPB-19	[010]	Dia. = 0.750", Th. = 0.375"	143	180

Figs. 14 and Fig. 15 shows the dynamic stress-strain responses in the [001] orientation for 0.5" dia. and 0.75" dia disk specimens, respectively.

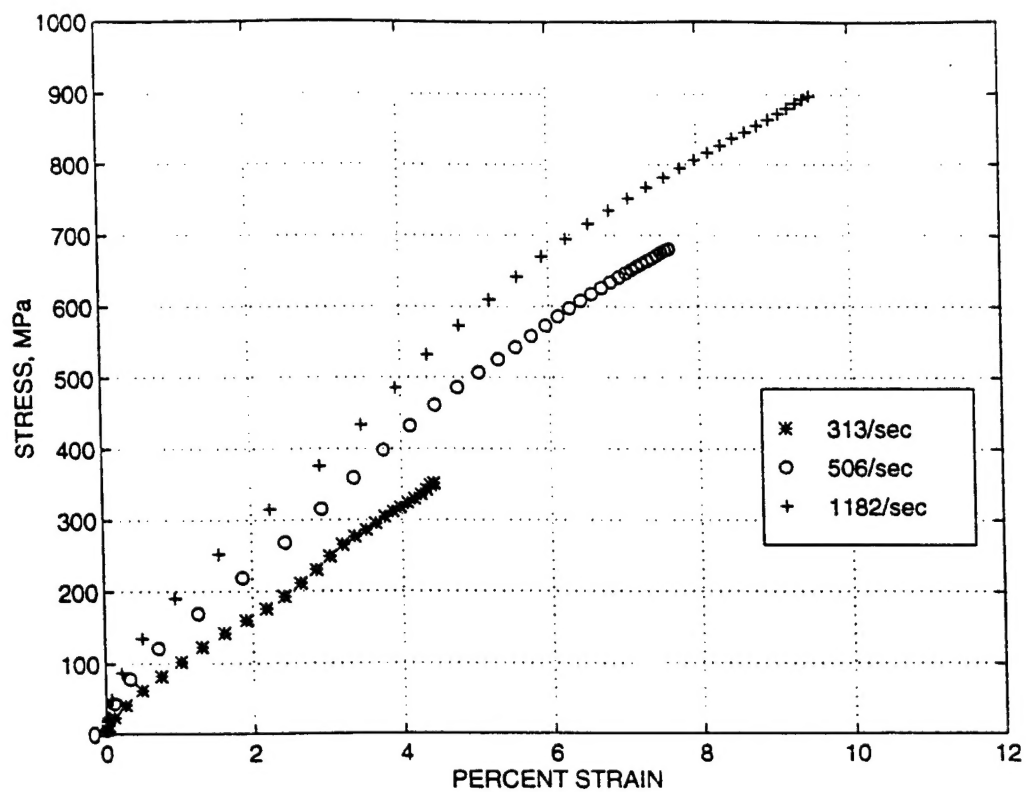


Fig.14 : Dynamic Response in [001] orientation(Specimen: 0.5" dia x 0.25")

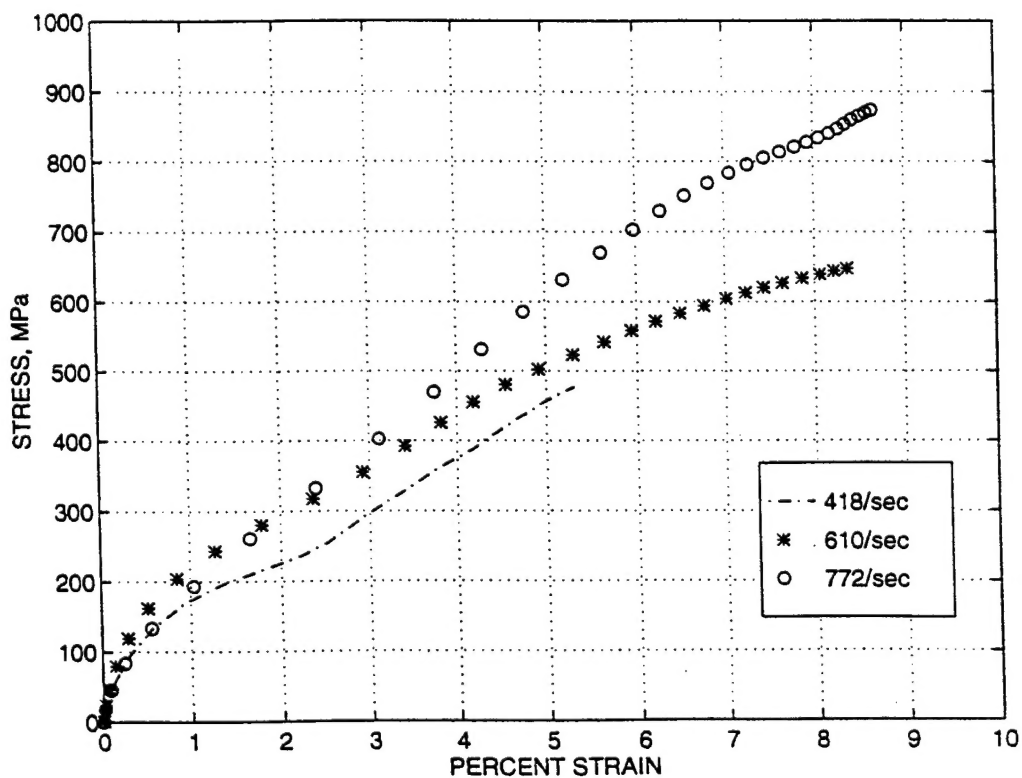


Fig.15 : Dynamic Response in [001] orientation(Specimen: 0.75" dia x 0.375")

As mentioned earlier, SHPB data in small deformation region (e.g. below 1.5%) is not reliable. As it was observed previously in quasi-static experiments, the specimen size has no or very little effect as seen from these two figures. Strain rate effect is prominently observed in both sizes of specimens. Another interesting observation is the strength of the material in the [001] orientation during dynamic loading is much higher. The average observed failure stress was noted to be around 930MPa at a strain rate of about 1182/sec. The failure strain was around 9.5%. In the ARL⁽²⁾ report, the failure stress was significantly different and was reported to be at 370MPa for a strain rate of 3000/sec. None of the larger diameter specimens failed as the stresses and strains had not reached the failure values. Three of the smaller diameter specimens failed at stresses of 910MPa, 924MPa and 970MPa but at the same strain of around 9.5%. The specimen failure mode was similar to that in the quasi-static experiments, resulting in two parts upon complete fracture. In one case, where the strain rate was greater than 1600/sec, the specimen failed with multiple fragments.

The [100] and [010] orientation specimens tested on Split Hopkinson Pressure Bar equipment did not show much difference in strength from that in the quasi-static tests. As the failure strains for these orientations are in the range of 1-1.5%, the stress-strain plots could not be considered very reliable. The failure stress observed was in the range of 180-270MPa. Although the failure stresses were quite similar to that in quasi-static loading, the failure mode was interestingly different. The specimen circular cross-section changed to an ellipse with the major axis in the direction of the ply layup. Upon reaching a maximum limit, delaminations began to occur and resulted in a failure. The number of delaminations occurring depended upon the strain rate and stress pulse magnitude.

CONCLUSIONS

Experiments were performed over a wide strain range in specimens with three orientation. The material behavior was found to be complex. In the two fiber directions, the response was almost elastic until failure with almost no strain rate sensitivity. Failure was observed to be mostly due to delaminations. In the thickness direction, i.e. perpendicular to fibers, moderately large visco-elastic deformations were observed. The elastic constants and failure stresses were significantly strain rate dependent. The failure mode was a combination of yarn fracture, matrix cracking and delaminations across shear planes. Black regions were observed on failed surfaces suggesting considerable temperature rise during failure.

REFERENCES:

1. P.K.Mallick; "Fiber Reinforced Composites"; Marcel Dekkel, NY, 1988.
2. S.C.Chou and E.deLuca, editors; "Dynamic Response of S-2 Glass Reinforced Structural Armor"; ARL Progress Report, Dec.1993.
3. T.W.Chou, F.Ko; "Textile Structural composites"; Elsevier Science Publishers, New York, 1989.
4. W.Chen, W.S.Kuo, A.Parvizi-Majidi and T.W.Chou; "Modeling and characterization of multi-directional reinforced ceramic matrix composites"; NASA Conference publication 10051, Paper no.76, 1990.
5. T.Ishikawa and T.W.Chou; "Stiffness and strength in behavior of woven fabric composites"; Journal of Material Science, 17, 1982.
6. T.Ishikawa and T.Chou; "Elastic behavior of woven hybrid composites"; Journal of composites materials, 16, 1982.
7. T.Ishikawa and T.W.Chou; "One dimensional micromechanical analysis of woven fabric composites"; AIAA Journal, 21, 1983.
8. Z.Wang, C.Laird, B.W.Rosen, Z.Hashin and C.F.Yen; "Mechanical behavior of cross weave ceramic matrix composite"; Journal of material science, 26, 1991.
9. N.K. Naik and P.S.Shembekar; "Elastic behavior of woven fabric composites", Journal of composite materials, Vol.26, 1992
10. N.K.Naik and V.K.Ganesh; "Failure behavior of plain weave fabric laminates under in plane shear loading"; American society for testing and materials, 1994.
11. M.Karayaka, P.Kurath; "Deformation and failure behavior of woven composite laminates"; Transactions of ASME, Vol.116, 1994.
12. P.Kumar and A.Garg; "Failure modes and fractographic study of glass-epoxy composite under dynamic compression"; Journal of material science, Vol 23, 1988.
13. I.M Daniel and J.W.Lee; "Damage development in composite laminates under Monotonic loading"; American Society of Testing and Materials; 1990
14. H.Z.Shan, P.Pluvnage, A.Parvizi-Majidi, T.W.Chou; "Damage mechanics of two-dimensional woven SiC/SiC composites"; Journal of Engineering materials and technology, Vol 116, 1994

15. W.Sachse and K.Y.Kim; "Quantative acoustic emission and failure mechanics of composites materials"; Ultrasonics, Vol 25, 1987.
16. K.Liao, B.Tang; "Evaluation of material variation in composite laminates by acoustic wave parameters"; Experimental Techniques ,1991.
17. D.S.Gardiner and L.H.Pearson; "Acoustic emission monitoring of composite damage occuring under static and impact loading";Experimental techniques, Nov.1985.
- 18.M.R.Gorman; "New technology for wave based acoustic emission and acousto-ultrasonics"; Wave propogation symposium, ASME Winter Annual Meeting, 1994.
19. C.M.Pastore and Y.A.Gowayed; "A self-consistent fabric Geometry model: Modification and application of a fabric geometry model to predict the elastic properties of textile composites"; American Society for Testing and Materials,1994.
- 20.K.Srinivasan,W.C.Jackson,B.T.Smith and J.A.Hinkley; "Characterization of damage modes in impacted thermoset and thermoplastic composites"; J. of Reinforced plastics and composites,1992.
21. B.N.Cox, M.S.Dadkhah, W.L.Morris and J.G.Flintoff; "Failure mechanisms of 3D woven composites in tension, compression and bending"; Acta metallica material, Vol.42,1994.
22. B.N.Cox and M.S.Dadkhah; "The macroscopic elasticity of 3D woven composites"; J. of composites materials, Vol29, 1995.
23. D.Bruno and A.Grimaldi; "Delamination failure of layered composite plates loaded in compression"; Intl. Journal of Solids & structures, Vol.26, 1990.
24. F.Chen, A.Hiltner and E.Baer; "Damage and Failure Mechanisms of continuous glasss fiber reinforced polyphenyle sulfide"; Journal of composite materials ,Vol.26, 1992.
25. L.M.Kachanov; Introduction to continuum damage mechaics; Martinus Nihhoff Publishers, 1986; Dordrecht, Netherlands.
26. D.Krajcinovic & J.Lemaitre,editors; "Continuum damage mechanics"; International centre for mechanical sciences, courses & lectures,No295, 1987;Springer Verlag 1987.
27. R.M.Christensen"Mechanics of composites materials";John Wiley & Sons,1979, NY,USA.